Capturing the breath of the heart by magnetic resonance imaging

Five-dimensional cardio-respiratory resolved cine imaging during free breathing

A doctoral thesis by

Karen Holst

Karolinska Institutet

Department of Molecular Medicine and Surgery

Stockholm 2017

Cover image: by Ryan McArthur.
Modified version of an original.

Published by Karolinska Institutet.
Printed by Eprint AB 2017

ISBN 978-91-7676-884-6

Capturing the Breath of the Heart by Magnetic Resonance Imaging

A doctoral thesis by

Karen Holst

Principal Supervisor
Andreas Sigfridsson, PhD
Karolinska Institutet
Department of Molecular Medicine and Surgery
Unit of Clinical Physiology

Co-supervisors
Martin Ugander, MD, PhD, Associate Professor
Karolinska Institutet
Department of Molecular Medicine and Surgery
Unit of Clinical Physiology

Kenneth Caidahl, MD, PhD, Professor
Karolinska Institutet
Department of Molecular Medicine and Surgery
Unit of Clinical Physiology

Opponent
Daniel Herzka, PhD
National Heart Lung and Blood Institute
National Institutes of Health
Bethesda, Maryland, USA

Examination Board
Jonas Svensson, PhD, Associate Professor
Lund University
Department of Translational Medicine
Unit of Medical Radiation Physics

Stefan Skare, PhD, Associate Professor
Karolinska Institutet
Department of Clinical Neuroscience

Erik Hedström, MD, PhD, Associate Professor
Lund University and Skåne University Hospital
Department of Clinical Sciences Lund
Clinical Physiology and Diagnostic Radiology

It is a bird-flight of the soul,
when the heart declares itself in song.

William Simms

To my beloved father who inspired me to pursue my dreams.

Abstract

Cardiac imaging with cardiovascular magnetic resonance has the advantage of enabling dynamic visualizations, several quantifiable measures, and good soft-tissue contrast. However, a major drawback is the need for breath holding during many acquisitions to limit motion artifacts. Breath holding is often insufficient for artifact reduction and, furthermore, limits the image acquisition to only one respiratory phase. The aim of this work, therefore, was to develop a free breathing cardiovascular magnetic resonance imaging method for three-dimensional whole-heart cine imaging to measure the left ventricular (LV) volume in all combinations of cardiac and respiratory phases.

Three-dimensional free-running acquisition was implemented as a double golden-angle radial trajectory. Respiratory self-gating signals were extracted from the center of *k*-space and used in combination with the measured electrocardiogram to bin data into combinations of cardiac and respiratory phase. Image volumes covering the whole heart were reconstructed and the LV endocardial border was manually segmented.

In the first of four studies (**Study I**), the proposed technique was validated for LV volumes in end diastole (EDV) and systole in end expiration against gold standard two-dimensional breath held cine imaging in healthy volunteers. No difference was found between the two methods with regard to LV volumes and in test-retest variability of the volume measurements. **Study II** focused on the respiratory cycle where the same free breathing acquisition was used for measuring the respiratory-induced variation in LVEDV and the acquisition time was reduced from 40 minutes to 4.5 minutes by implementing parallel image reconstruction. The maximum respiratory variation in LVEDV was found to be 5-6% for healthy volunteers. An extension to the double golden-angle acquisition was implemented in **Study III** to reduce eddy current-induced artifacts, which improved image quality. A projection-based respiratory self-gating strategy was added to the improved trajectory in **Study IV** and used to measure respiratory variation in LVEDV in consecutive patients referred for cardiac evaluation with cardiovascular magnetic resonance imaging. In patients, the *k*-space based self-gating failed to measure the respiratory variation in LVEDV, whereas with the projection based self-gating yielded an 8% respiratory variation in LVEDV.

In conclusion, this work presents a novel method for measuring the LVEDV resolved in a two-dimensional cardio-respiratory phase map and provides three-dimensional isotropic-resolution image volumes enabling multiple view angles of the heart in one acquisition.

List of Scientific Papers

The following papers form the basis for this thesis. They are the results of four studies (Studies I-IV) and will be referred to by their roman numbers in Chapters 1 through 6.

I. Left Ventricular Volume Measurements with Free Breathing Respiratory Self-Gated 3-Dimensional Golden Angle Radial Whole-Heart Cine Imaging – Feasibility and Reproducibility

Holst K, Ugander M, Sigfridsson A
Magn Reson Imaging 2017;43:48–55

II. Respiratory Variation in Left Ventricular Cardiac Function With 3D Double Golden-Angle Whole-Heart Cine Imaging

Holst K, Ugander M, Sigfridsson A
Magn Reson Med 2017. doi: 10.1002/mrm.26942

III. Generalization of Double Golden-Angle Three-Dimensional Radial Acquisition to Reduce Eddy Currents in Free-Breathing Cardiac bSSFP Cine Imaging

Holst K, Fyrdahl A, Caidahl K, Ugander M, Sigfridsson A
Submitted

IV. Respiratory Resolved Whole-Heart Imaging in Patients with Free Breathing Tiny Golden-Angle 3D Radial Acquisition

Holst K, Fyrdahl A, Caidahl K, Ugander M, Sigfridsson A.
Manuscript

Contents

List of Abbreviations

1D, 2D, … XD	X-Dimensional
bSSFP	Balanced Steady-State Free Precession
CMR	Cardiovascular Magnetic Resonance
ECG	Electrocardiogram
EDV	End Diastolic Volume
EF	Ejection Fraction
ESV	End Systolic Volume
LV	Left Ventricle
M-mode	Motion-mode
MRI	Magnetic Resonance Imaging
NAV	Navigator
NMR	Nuclear Magnetic Resonance
RF	Radio Frequency
SA	Short Axis
SV	Stroke Volume

Chapter 1
Introduction

It pumps, and pumps, and pumps, and pumps, and … suddenly it doesn't pump as well anymore. We only *then* notice its importance. The heart is one of the most enduring organs we have in our bodies, and its job is to work hard all our life without claiming much attention to the fact that it even exists. It tirelessly works in collaboration with the lungs to deliver oxygen and nutrients to hungry cells. But sometimes it is hit by disease and we need to act efficiently to find the cause so it can be treated.

Cardiac diseases are rapidly growing in prevalence worldwide and pose a major challenge to health sectors and researchers to develop new diagnostic tools as well as improve existing tools. Cardiovascular magnetic resonance (CMR) has increasingly gained ground as a diagnostic method because it offers a complete combination of dynamic and functional visualizations, quantifiable measures, tissue characterization and high soft-tissue contrast. However, CMR is considered to be inferior to ultrasound and CT in terms of acquisition times and suffers from many sources of image artifacts.

Among these limitations is breath holding. It is used to reduce image artifacts caused by respiratory motion; yet, when performed in an insufficient manner, image artifacts are still the result. Free breathing CMR methods are rapidly emerging and show great promise in improving cardiac imaging. The heart lies directly on top of a large respiratory muscle, the diaphragm, and when this moves up and down the heart moves with it. Consequently, many of the free breathing methods focus on determining the location of the heart during respiration. However, the interaction between the heart and respiration is more complex than a simple change in position. Respiration is enabled by large pressure changes in the chest that not only cause air to be inhaled and exhaled, but also influences the filling of the cardiac chambers that many free breathing techniques fail to account for.

Furthermore, the majority of existing free breathing methods imitate the purpose of breath holding to image the heart in a single respiratory phase. But with free breathing CMR, visualization of the heart in more than a single respiratory phase is possible.

Patients with constrictive pericarditis and restrictive cardiomyopathy present with similar symptoms but need very different treatments. One of the few measurable differences between these diseases is the respiratory variation in interventricular coupling, and these patients would therefore benefit from whole-heart free breathing CMR.

A standard CMR exam often takes more than 45 minutes and requires a high level of co-operation between the patient and technologist. A large part of the exam consists of acquiring two-dimensional (2D) image slices in different angles and stacks of 2D images to cover the whole heart, most of them acquired during breath holding. Though the complete freedom to acquire any image orientation is part of the advantage with magnetic resonance imaging (MRI), it is prone to error as it is highly operator-dependent and requires a substantial amount of time to plan each scan position. This often causes decreased image quality due to either an unfortunate acquisition plan or poor breath holding. Cine images are a central element of the CMR exam, used for quantification of essential functional parameters such as left ventricular (LV) volumes and ejection fraction (EF).

There is, therefore, a definite need for a free breathing acquisition technique that covers the whole heart in three dimensions (3D) and allows for retrospective assessment of image slices at any angle through the heart. Such a method would eliminate the need for breath holding and simplify the scan strategy of the CMR exam. A free breathing technique would furthermore be useful in specific diseases, such as those involving stiffness changes of the myocardium or pericardium, where the normal pattern of respiratory variation in cardiac dimensions is changed.

1.1 Thesis and study aims

The overall aim of this thesis was to develop and validate a CMR method for free breathing whole-heart cine imaging allowing for measurements of LV volume resolved over both the cardiac and respiratory cycles.

Specific aims for Studies I-IV were:

I. To validate LV volumes, measured with free breathing 3D cine imaging against standard breath held 2D cine imaging in healthy individuals.

II. To measure the respiratory-induced variation in LV end-diastolic volume in healthy individuals with reduced scan time.

III. To reduce eddy current-related artifacts for the time-resolved 3D CMR acquisition sequence.

IV. To evaluate a new respiratory self-gating method and measure the respiratory-induced variation in LV end-diastolic volume in patients.

1.2 Method design requirements and thesis content

Design requirements for the CMR method to fulfill above aims were as follows:

- Three-dimensional acquisition for whole-heart imaging
- Free breathing
- Continuous acquisition to optimize acquisition time
- Ability to retrospectively extract information about respiratory motion
- Data binning in the two-dimensional cardio-respiratory phase map
- Smart image reconstruction for undersampling and limiting the acquisition time

The result was *five-dimensional cardio-respiratory resolved cine imaging during free breathing*.

To understand the importance of free breathing whole-heart cine imaging, a description of the cardiac physiology and function as well as the normal cardio-respiratory coupling and diseases affecting the respiratory variation in cardiac function is described in Chapter 2. Chapter 3 contains a brief introduction to magnetic resonance acquisition and image reconstruction, challenges with imaging the heart as well as a description of the acquisition method satisfying the above design requirements. Chapter 4 concerns the extraction of respiratory motion, cardio-respiratory data binning and, finally, some results from visualizing the cardio-respiratory coupling. A discussion is found in Chapter 5 and final conclusions in Chapter 6.

Chapter 2

Cardio-Respiratory Physiology

The heart and lungs are two dynamic organs that work tirelessly to provide the rest of the body with oxygen so the cells and tissues can perform their tasks. By constantly pumping, the heart is supplying blood with oxygen, nutrients and other vital substances through arteries to a network of capillaries where exchange between cells and blood occur. Carbon dioxide and other waste products are carried away with the blood through veins to be dealt with by other organs. The vascular system has two independent and closed circulatory systems (Figure 2.1) which was discovered by William Harvey in 1628 (1). Transportation of blood from the heart through the tissues and back to the heart describes the systemic circulation. The pulmonary circulation runs from the heart through the lungs, where the blood is oxygenated and carbon dioxide is disposed before it is led back to the heart and continues into the systemic circulation.

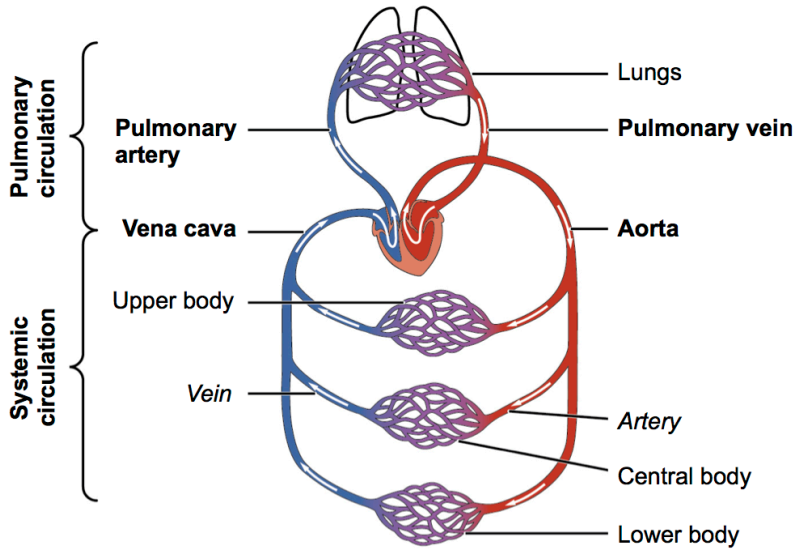

Figure 2.1 Diagram of the circulatory system. Two closed loops form the systemic circulation and he pulmonary circulation. The systemic circulation receives oxygenated blood (red) from the left side of the heart and returns deoxygenated blood (blue) after use in the capillary network to the right side of the heart. The pulmonary circulation receives deoxygenated blood from the right side of the heart and return oxygenated blood to the left side of the heart. *Image obtained and modified from OpenStax CNS.*

The heart and lungs both lie inside the enclosed thoracic cavity, as illustrated in Figure 2.2, and are therefore not only connected through the vascular system, but also by the forces acting inside the thoracic cavity during respiration (2,3). In Section 2.1 and 2.2 the normal heart and respiratory system are described separately and the cardio-respiratory coupling will be explored in Section 2.3. Section 2.4 gives a short description of how the cardio-respiratory coupling is affected in some diseases.

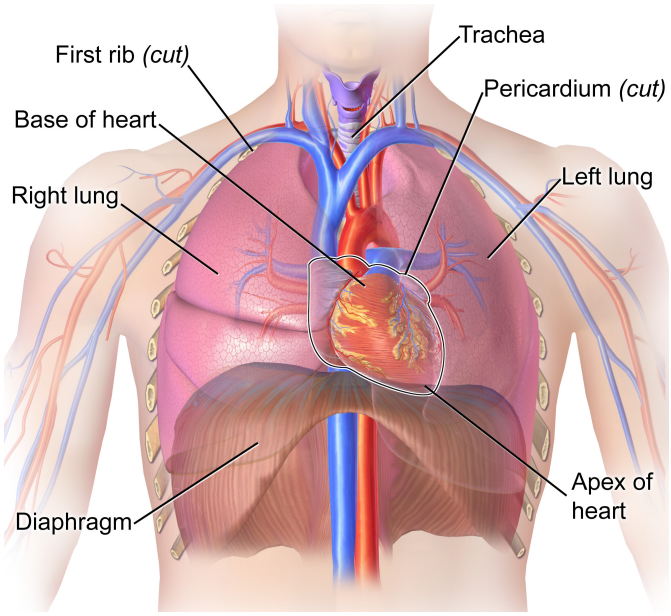

Figure 2.2 Illustration of the lung and heart position inside the thoracic cavity. *Image obtained and modified from Medical Gallery of Blausen Medical 2014.*

2.1 The normal heart

2.1.1 Anatomy and function

The heart is well protected inside the ribcage and is resting on top of the diaphragm between the lungs. It has two sides, completely separated by a septum, which each receives the blood from one circulation and pumps it into the other circulation (see Figure 2.3) (4). The right side receives deoxygenized blood from the systemic circulation through the superior and inferior vena cava and ejects it into the pulmonary trunk for oxygenation in the lungs. The left side receives oxygenized blood from the pulmonary circulation through the pulmonary veins and ejects it into the systemic circulation through the Aorta. Each side of the heart is divided into two chambers, an atrium and a ventricle, which contract separately.

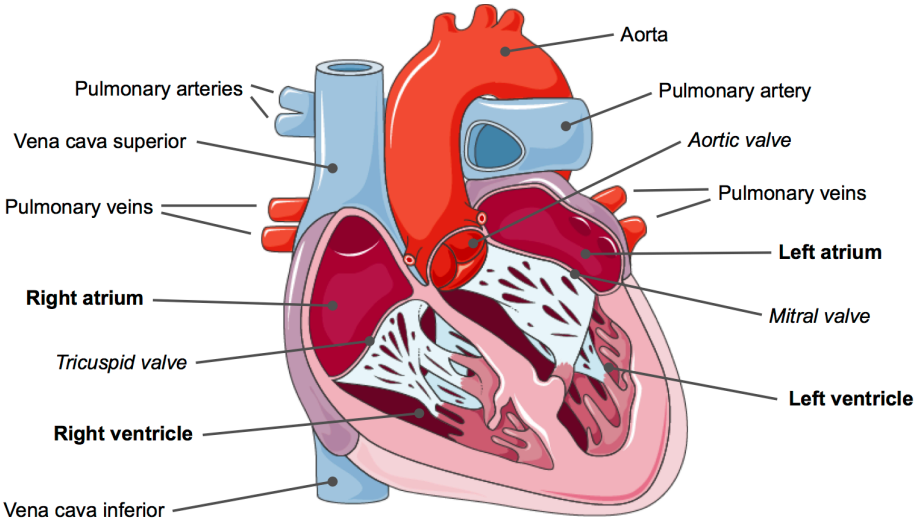

Figure 2.3 Cross section of the heart showing the four chambers: right and left atria and ventricles, the large vessels going into the heart: vena cava superior and inferior and the pulmonary veins as well as the large vessels going out from the heart: aorta and the pulmonary trunk. Only three of the four valves are visible. *Image obtained and modified from Servier Medical Art.*

Four valves, all positioned in the atrioventricular plane, ensure that the blood only flows in one direction when the heart contracts (4). The atrioventricular plane forms the base of the ventricles and is illustrated in Figure 2.4. On the right side of the heart, the flow from the atrium to the ventricle is directed by the tricuspid valve and from the ventricle to the pulmonary trunk by the pulmonary valve. On the left side, the flow from the atrium to the ventricle is directed by the mitral valve and from the ventricle to the aorta by the aortic valve.

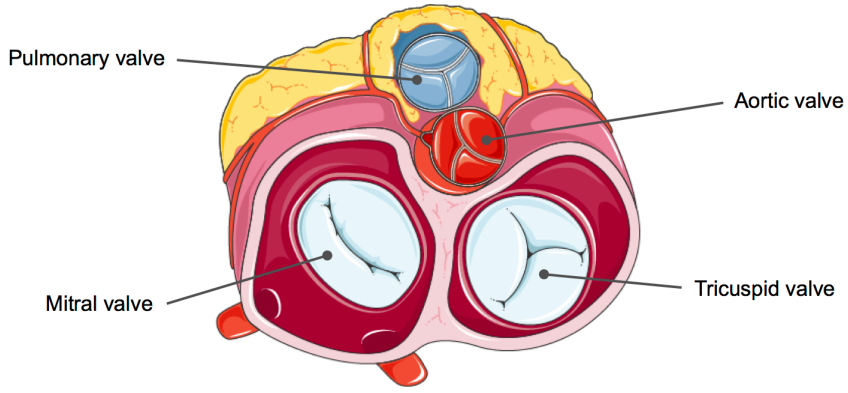

Figure 2.4 Illustration of the atrioventricular plane forming the base of the ventricles. *Image obtained and modified from Servier Medical Art.*

Myocardium, which makes up the heart wall, creates a contraction force when the specialized cardiac muscle cells are activated (5). Contraction of the myocardium is initiated through an electrical conduction system in the heart itself with a complex integrated control by the nervous system (6).

Like all other organs, the heart is dependent on oxygen and has its own blood supply through the coronary arteries that branches out from the stem of the aorta and runs along the outside of the myocardium (4). The heart is enclosed in the pericardium (Figure 2.5), which consists of two membranes with a serous fluid that reduces the friction during contractions between the heart and surrounding structures as well as holds it in place in the thoracic cavity. An endocardial layer covers the inside of the chambers (4).

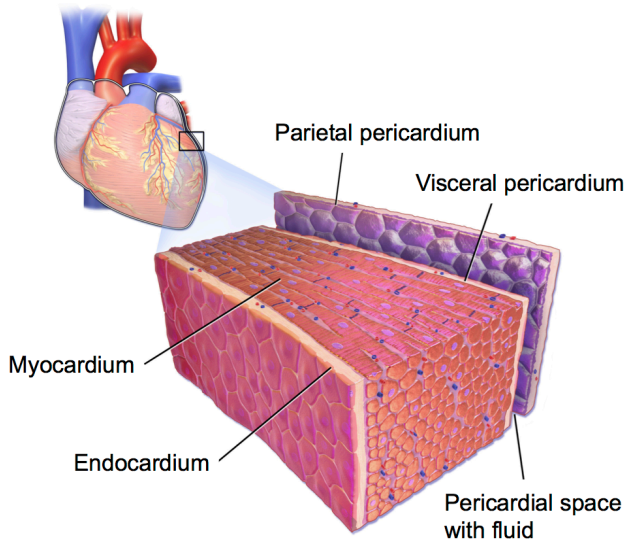

Figure 2.5 Illustration of the pericardium forming the outer layer of the heart. Between the parietal and visceral pericardial layers is the pericardial fluid which allows frictionless contraction of the heart. *Image obtained and modified from Medical Gallery of Blausen Medical 2014.*

2.1.2 Physiology and the cardiac cycle

Creating blood flow and regulating the blood supply is the heart's main purpose, in order to ensure the distribution of oxygen and nutrients to the body. The flow is a result of myocardial contraction, which increases the pressure in the chambers and ejects the blood into circulation. Continuous pumping of the heart happens in cycles of ventricular filling, diastole, and ventricular contractions, systole (7). Because the resistance in the systemic circulation is considerably higher than in the pulmonary circulation, the left ventricular wall is thicker than the right.

Figure 2.6 shows a schematic of the electrocardiogram (ECG) that can be measured on the surface of the chest with electrodes. The ECG measures the activity in the electrical conducting system of the heart and the small ion-driven action potentials of the myocytes (muscle cells) themselves (8). During the cardiac cycle, blood is moved through the heart by pressure changes causing blood to move from chamber to chamber. Figure 2.7 shows a Wiggers diagram (9) illustrating the pressure and volume changes happening in the left side of the heart during the cycle in relation to the ECG and phonogram. In the phonogram the sounds of the closing valves divide the ventricular systole and diastole.

Ventricular systole is visible in the ECG as the QRS complex where electrical signals rapidly spread through the ventricles, making them contract. Systole starts at closings of the mitral and tricuspid valves when ventricular pressures exceed that in the atria. Ending of systole is marked with closings of the aortic and pulmonary valves after ejection into the circulations (9). The aortic and pulmonary valves close when the ventricles start relaxation (T-wave in the ECG) and the ventricular pressure drops below the aortic and pulmonary trunk pressures.

Systole is followed by diastole, which happens in three phases: early diastole, diastasis and atrial contraction (10). During early diastole the ventricles expand as they relax, causing the mitral and tricuspid valves to open when the ventricular pressure drops below that in the atria. In early diastole the ventricles are filled passively due to the negative pressure gradient relative to atrial pressure and accounts for the majority of ventricular filling (11). Diastasis occurs when the ventricular pressure is equal to the atrial pressure and there is virtually no change in the ventricular volume and no motion of the heart. When atrial contraction is initiated (P-wave in the ECG), more blood is forced into the ventricles and marks end diastole when the ventricular volume is largest during the cardiac cycle. Atrial contraction is closely followed by initiation of ventricular contraction as a new cycle starts.

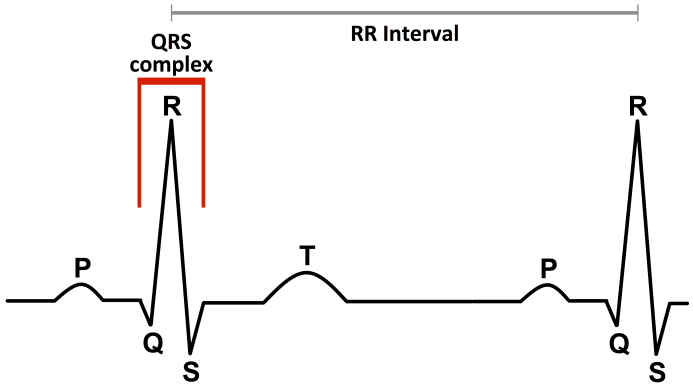

Figure 2.6 Diagram of an electrocardiogram showing the different phases. During the QRS complex, systolic contraction is initiated, the T wave represents beginning of diastole and the P wave is atrial contraction.

Understanding the different phases of the cardiac cycle is of great importance for imaging technologies. As an example LV volume might be highest in the very end of diastole, but has the disadvantage that the atrium is contracting, the ventricle is increasing slightly in size and the blood is moving. Compared to other imaging technologies, CMR is relatively slow in data acquisition and is therefore sensitive to motion. For more robust and reproducible imaging it might therefore be a better trade-off to acquire images in the diastasis part of diastole as was done in Study II and Study IV.

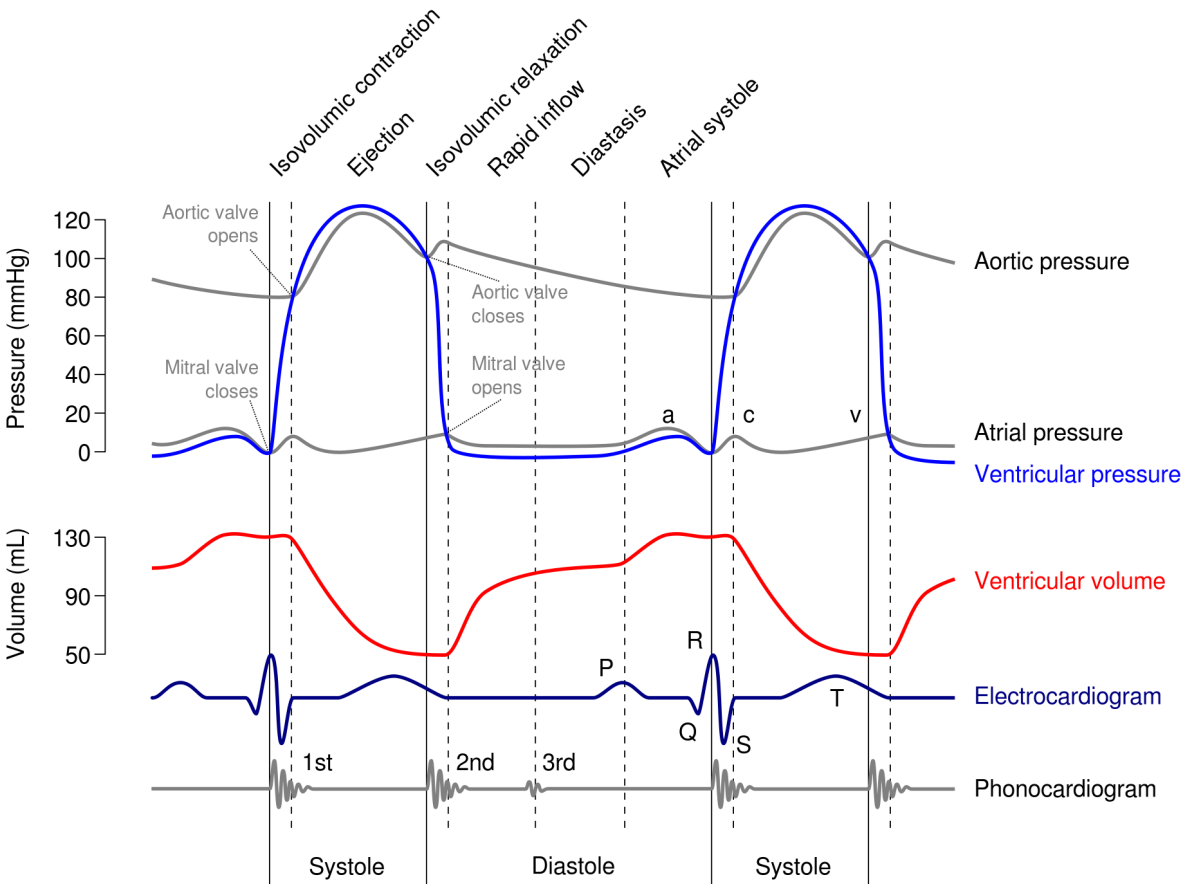

Figure 2.7 Wiggers diagram showing left atrial, LV and aortic pressures during the cardiac cycle (top) compared to the LV volume, ECG and phonocardiogram. Specifically notice the plateau of ventricular volume in the diastasis phase of diastole and the low atrial pressure throughout the entire cycle. *Image obtained and modified from Wikimedia Commons by DanielChangMD and DestinyQx.*

Heart rate (HR) and contraction force are adapted to changing needs of oxygen supply by stimulations from the brain stem. The brain stem receives various nerve and hormone inputs that either inhibit or stimulate a change in blood pressure (12). The collective of all these inputs is signaled to the sinoatrial node that transmits the information through the cardiac conducting system. Blood pressure is controlled by the cardiac output, which is defined as the blood volume per minute leaving the heart, and the performance of the heart is therefore vital for continuous homeostasis. The condition of the heart is in clinical settings therefore often assessed by measuring the ventricular volumes in end diastole and end systole, and most often the left ventricle is in focus since it carries blood into the high-resistance systemic circulation. The LV end-diastolic volume (EDV) is ideally measured immediately before the mitral valve closes and the LV end-systolic volume (ESV) immediately before the aortic valve closes when the ventricle as at its smallest. LV stroke volume (SV) is given as

$$SV = EDV - ESV \ (mL) \tag{1}$$

and the cardiac output (CO) as

$$CO = SV \cdot HR \ [mL / min] \quad (2)$$

Cardiac output is, however, not often used as a direct clinical measure. Cardiac function is more often assessed from SV and ejection fraction, with EF given as

$$EF = SV / EDV \ [\%] \quad (3)$$

Left ventricular EDV, ESV, SV and EF are standard parts of a clinical CMR assessment and the measures used in Study I to validate the method against a standard breath held imaging method.

2.2 The normal respiratory system

2.2.1 Anatomy and function

Metabolic processes in the cells are dependent on a constant supply of oxygen and removal of carbon dioxide. The lungs are responsible for the gas exchange and ventilate the blood through continuous cycles of inspiration and expiration (10). They are positioned inside the thoracic cavity on each side of the heart and are attached on top of the diaphragm and beneath the ribcage (see Figure 2.2) (4). The trachea connects the lungs to the exterior via the mouth and nose.

Airflow between the exterior and the lungs is facilitated by changes in thoracic cavity size thereby creating pressure gradients. The diaphragm together with intercostal muscles are the main respiratory muscles. The diaphragm is responsible for the majority of respiration at rest; it makes up the entire bottom of the thoracic cavity and divides this from the abdomen. Intercostal muscles between the ribs facilitates in- and expiration. Accessory muscles (neck and back muscles) are activated when oxygen demands increase, for example during exercise (10). Because the lungs are attached to the diaphragm and ribcage, they expand in volume when the diaphragm contracts and pulls the lungs downward or the intercostal muscles contract and pulls the ribcage outward, as illustrated in Figure 2.8.

The lungs are encapsulated in a layer of pleura that provide attachment to the inside of the ribcage and diaphragm as well as reduce friction when the lungs are expanding and decreasing. The pleura consists of a membrane attached to the lung surface, a membrane attached to the inside of the ribcage and top of the diaphragm and a thin layer of visceral pleural fluid in between. The pleural cavity has a small negative pressure of approximately 4 mmHg, also called the intra-thoracic pressure (4,10).

Contraction of the respiratory muscles is stimulated and regulated from the brain stem as a collective of inhibiting or stimulating inputs from the rest of the body (13).

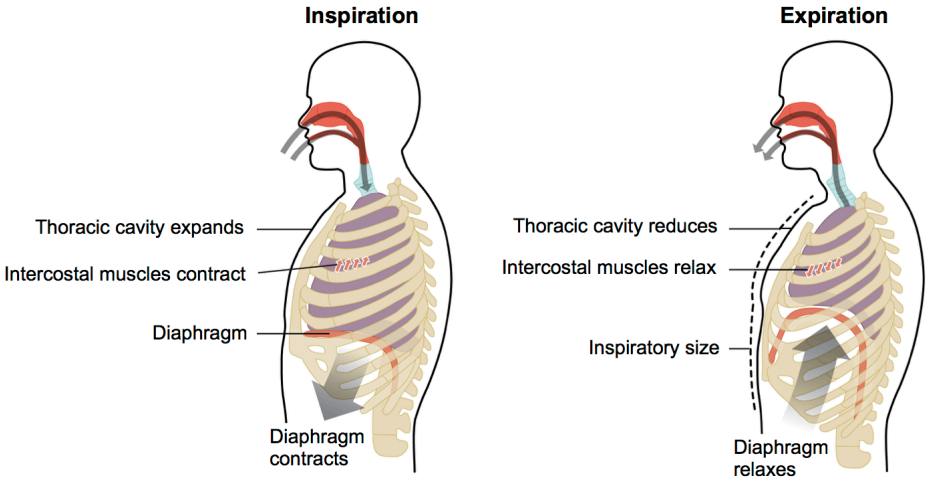

Figure 2.8 Inspiration and expiration are controlled by contraction and relaxation of the diaphragm and intercostal muscles. Contraction of the muscles expands the chest for inspiration and relaxation allows the recoil properties of lung tissue to compress the chest.

2.2.2 Respiration

At rest, oxygen is only needed to sustain a basic level of activity. Breathing feels easy and only use a fraction of the total lung capacity. But in situations of higher demand the respiratory system has an enormous capacity to increase the oxygen intake and expulsion of carbon dioxide. Figure 2.9 illustrates the change in lung volume during respiration at rest and when the full inspiratory and expiratory reserve volume is used.

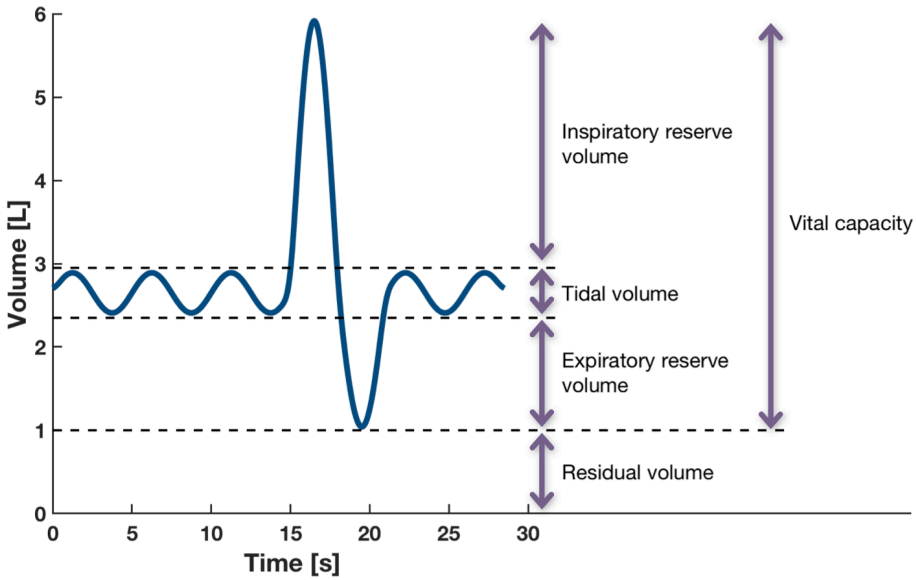

Figure 2.9 Lung volume during normal respiration. Tidal breathing happens during rest and when oxygen demand increases the inspiratory and expiratory reserve volumes are used. Note that the slope of the respiratory volume curve is flow and reflects respiratory pressure.

Respiratory volume at rest, the tidal volume, is approximately 500 mL for young healthy individuals (14). This can increase in situations of high demand, however, and the respiratory vital capacity is around 3.1 L in women and 4.8 L in men. Approximately 1 L during maximum respiration is never expired which ensures that the lungs do not collapse (15).

Inspiration starts with contraction of the respiratory muscles, causing an increase in thoracic volume, followed by a pressure drop inside the lungs, creating a negative pressure gradient between the lungs and the exterior, resulting in air being sucked into the lungs. The negative pressure in the pleural cavity plays a major role in ensuring the expansion of the lungs. In expiration the respiratory muscles relax, followed by elastic recoil of the lung tissue, which increases the pressure and forces air out of the lungs (10). During tidal breathing, the point of end expiration happens when the respiratory muscles are completely relaxed and the elastic properties of the lung tissue create a pressure balance between the lungs and the exterior. In end expiration the pressure gradient is zero and equilibrium is reached. Breath holding in CMR is for this reason done at end expiration to ensure as stable a situation as possible.

Normal breathing varies in frequency and magnitude and Figure 2.10 shows an example of respiratory patterns in two young healthy individuals. The top respiration shows how rapidly the frequency can change in one individual as well as the scale of the change. The bottom shows an example from another young healthy individual that has a much more consistent respiratory pattern. Both of these patterns are normal and also vary within one individual over the course of a single day or even a few minutes.

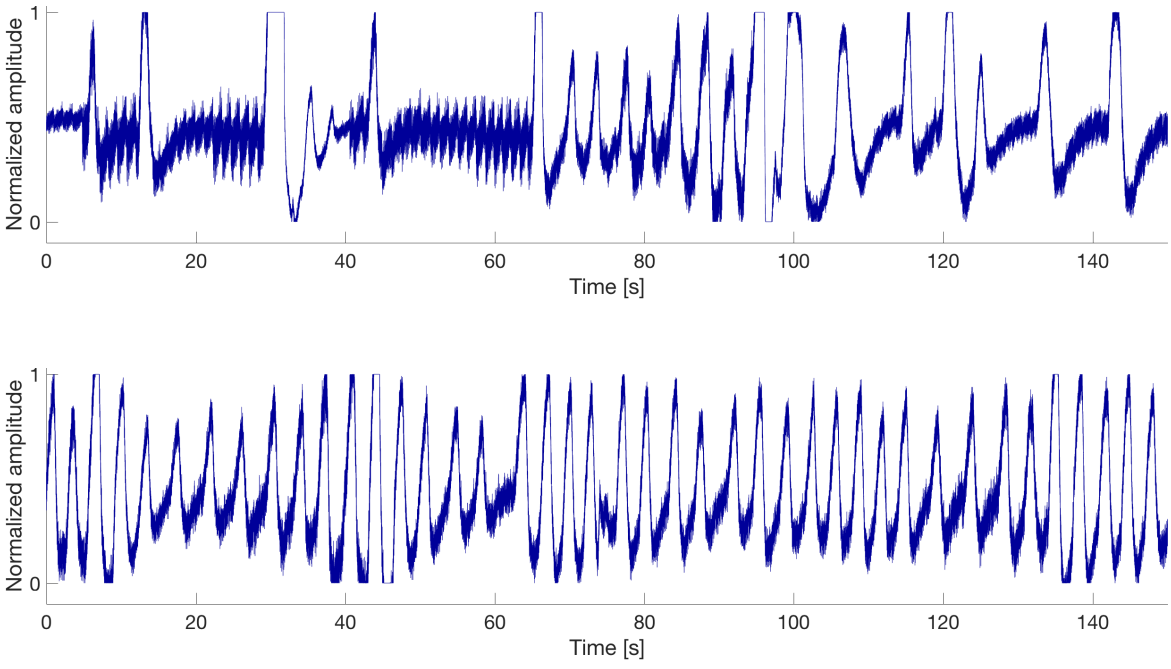

Figure 2.10 Examples of respiration measured with respiratory bellows from healthy volunteers. Both the top and bottom curves illustrate the variation in normal respiration.

2.3 Coupling between the heart and the respiratory system

Both cardiac pumping and respiration are mechanically complex systems and their location in the same enclosed cavity makes it unavoidable that they affect each other. Both mechanical processes involve passive flow of either blood or air in reaction to pressure changes. In the heart, negative ventricular pressure in early diastole is responsible for the majority of ventricular filling. In a similar fashion, negative pressure in the lungs causes airflow from outside the body into the lungs, and positive pressure causes the air to flow out of the lungs.

The difference between these two situations is, however, that the ventricular pressure only affects the arterial and venous flow but the respiratory pressure affects the entire thoracic cavity. The thoracic volume can change dramatically during respiration, with most of this effect contained to the inside the lungs as they expand or decrease. But the intra-thoracic space outside the lungs is also affected in part, including the large vessels going into and out from the heart. Small variations of a few mmHg in the negative pleural pressure during respiration are responsible for the variation in the volume of the thoracic cavity. In the following sections we will take a closer look at how inspiration and expiration affect the cardiac function.

In systole, the ventricular pressures far exceed the intra-thoracic pressure, and the respiratory-induced pressure change therefore has a negligible effect on ventricular ejection. Furthermore, the walls of the aorta and the pulmonary trunk are thick and can withstand high pressures. The ventricular filling pressure in early diastole, however, is much lower and therefore more likely to be affected by changes in intra-thoracic pressure (16).

The right ventricle receives blood from the systemic circulation via the atrium, most of it from outside the thoracic cavity. Right atrial pressure is typical 2 mmHg and only varying slightly during the cardiac cycle (10). Respiratory variation in intra-thoracic pressure is only a few mmHg, but produces a detectable variation in right atrial pressure and thereby filling of the right ventricle. This entails that venous return to the right atrium is increased during low-pressure inspiration (blood is sucked into the thoracic cavity) and reduced during high-pressure expiration (see Figure 2.11).

Left atrial pressure is normally 4-12 mmHg and the variation in intra-thoracic pressure therefore only has minimal impact on LV filling pressure. However, left ventricular filling is indirectly affected by the respiratory variation through the interventricular septum. During inspiration, the increased right ventricular filling pushes the interventricular septum towards the left and thereby restricts left ventricular filling. The opposite occurs during expiration, whereby the right ventricular filling is reduced and this allows the septum to shift right, which increases left ventricular filling. The ventricles are thus coupled by septal movement, and experience an opposite respiratory-induced

variation in EDV as illustrated in Figure 2.11. It has been shown that the normal respiratory-induced septal excursion is approximately 7 % relative to the biventricular diameter (17).

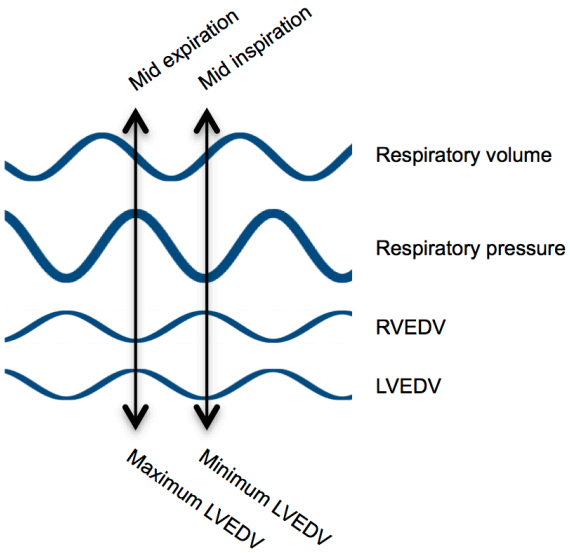

Figure 2.11 Respiratory volume in comparison to respiratory pressure and ventricular EDV. The phase shift between respiratory pressure and respiratory volume illustrates how the minimum and maximum pressures occur in mid inspiration and mid expiration, respectively. The right ventricular (RV) EDV and LVEDV have opposite phase because of the interventricular coupling.

2.4 Diseases affecting the cardio-respiratory coupling

The cardio-respiratory coupling affects ventricular diastolic filling. Right ventricular filling is directly affected by the intra-thoracic pressure, and left ventricular filling through the interventricular coupling. Diseases affecting the filling pressure of the right ventricle therefore potentially affect the normal respiratory variation in cardiac dimensions. It is not the scope if this thesis to present a full review of diseases affecting the cardio-respiratory coupling, but one brief example is given here to emphasize the importance of visualizing and measuring the respiratory variation in cardiac function.

Pathological stiffness changes of the myocardium or pericardium are examples of conditions where the ventricular filling is impaired due to loss of compliance (18). Both the myocardium and pericardium possess elastic properties to allow expansion of the ventricles in diastole (19) and stiffening of either of them therefore leads to impaired diastolic function and thereby potentially changes in the cardio-respiratory coupling.

Constrictive pericarditis and restrictive cardiomyopathy are diseases that present with very similar symptoms and hemodynamic findings. Therefore it is difficult to differentiate between the two conditions. However, the loss of compliance leading to impaired diastolic filling has different impact on the septal excursion during respiration,

which therefore can be used to set the correct diagnosis (20). Due to the different nature of the diastolic impairment, they demonstrate different respiratory variation in the interventricular coupling (21).

Constrictive pericarditis is caused by inflammation that thickens the pericardium, followed by a loss of compliance and scaring that constricts the relaxation and expansion of the heart in diastole (22). Constrictive pericarditis is usually curable and requires surgery (23).

Restrictive cardiomyopathy is an infiltrative disease affecting the myocardium caused by e.g. fibrosis and results in a loss of compliance in the myocardium (22). Diastolic filling is impaired in a similar way to constrictive pericarditis (18), but restrictive cardiomyopathy can only be treated medically which is why differentiating the two is crucial.

In early diastole, opening of the tricuspid valve normally happens sooner than the mitral valve, which in constrictive pericarditis leads to exaggeration of the respiratory-induced septal excursion (24). The loss of pericardial compliance constricts the ventricles ability to expand during diastole and the right ventricular pressure increases rapidly, thus forcing the interventricular septum further towards the left than is the case in normal individuals. In restrictive cardiomyopathy, a similar pressure increase happens in early diastole, but the loss of compliance happens in the myocardium itself, including the interventricular septum that becomes more rigid and unable to move (17). No change, or even a decrease, in the interventricular coupling is found in restrictive cardiomyopathy (17,25).

Determination of the respiratory variation in cardiac dimensions could therefore enable differentiation between constrictive pericarditis and restrictive cardiomyopathy.

Chapter 3
Magnetic Resonance Imaging

Magnetic Resonance Imaging is based on the principle of nuclear magnetic resonance (NMR) (26) and is used for non-ionizing and non-invasive imaging of all parts of the human body. Cardiac imaging with MRI poses several challenges that are particular compared to imaging other parts of the body, and cardiovascular magnetic resonance is therefore a specialized sub-field of MRI. In this chapter, we will briefly go through the general principles of MRI in Section 3.1, a short description of cardiac cine imaging is given in Section 3.2 and some of the challenge of respiratory motion are presented in Section 3.3. A deeper insight into 3D CMR trajectory design is provided in Section 3.4. Finally, specific elements of image formation relevant to the work behind this thesis can be found in Section 3.5.

3.1 Principles of magnetic resonance imaging

Figure 3.1 shows a schematic illustration of an MRI scanner. It consists of three main elements: a static magnetic field, gradient coils and a radio frequency (RF) coil. The static field, B_0, is created by a superconducting electromagnet cooled with liquid Helium to a temperature of 4 Kelvin. Most clinically available MRI scanners have a B_0 field of 1.5 Tesla (T) or 3 T, but higher field strengths are emerging on the market. The research presented here is all done using a 1.5 T scanner.

3.1.1 The MRI signal

A magnetic resonance signal can be obtained from nuclei of atoms possessing the physical property of spin angular momentum (26). Nuclei with an odd number of protons and/or an odd number of neutrons possess spin angular momentum that gives them a precession when subjected to a magnetic field (26). Hydrogen is by far the most commonly used nucleus in MRI since it exists in abundance in the human body, bound in water and a number of other molecules. All notions of MRI in the rest of this thesis will refer exclusively to hydrogen based imaging.

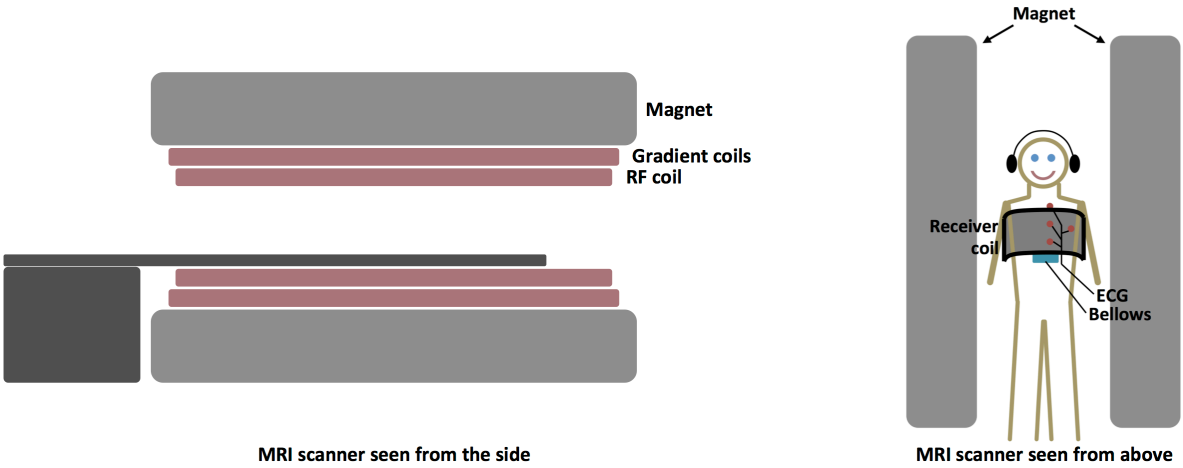

Figure 3.1 Diagram of an MRI scanner in cross-section of the scanner bore. *Right: obtained and modified from the authors previous Master's thesis.*

When an object containing hydrogen is positioned inside an MRI scanner bore, all hydrogen nuclei, also called spins, tend to align with the magnetic B_0 field where they experience the lowest energy state (27). The alignment happens through a precessing motion perpendicular to the B_0 field with a precession angular frequency, ω, proportional to the magnetic field strength with

$$\omega = \gamma \cdot B_0 \tag{4}$$

where the proportionality constant, γ, is the gyromagnetic ratio and ω is called the Larmor frequency (28). For hydrogen the gyromagnetic ratio is $42.6\ \mathrm{MHz/T}$, thus the precession frequency in a 1.5 T field is $42.6\ \mathrm{MHz/T} \cdot 1.5\ \mathrm{T} = 63.9\ \mathrm{MHz}$.

In a static magnetic field, the spins are in equilibrium and no signal is produced. A signal can only be obtained after the spins are brought away from the equilibrium through excitation by electromagnetic radiation with a frequency exactly matching that of the precession, i.e. the Larmor frequency (29). The Larmor frequency of the hydrogen nuclei falls in the RF range and the excitation pulses are therefore referred to as RF pulses. Coherent precession of spins immediately after excitation induces currents in the receiver coils, which is the NMR signal used for imaging. Immediately after the excitation, the spins begin to relax, i.e. return to the equilibrium, and the signal decays.

The rate of the relaxation depends on how the hydrogen nuclei are bound as well as how they are interacting with other molecules in their surroundings. Differences in the relaxation between tissues are the source of image contrast. The complex nature of the relaxation process is not within the scope of this thesis, but more information can be found in (27).

The RF signal from the hydrogen nuclei is typically received by surface coils positioned in close proximity to the volume of interest. These surface coils consist of

several coil elements each providing some unique information about the received signals that later can be used in the image reconstruction process.

3.1.2 Spatial encoding

The signal that can be measured after excitation is generated by the sum of all the spins that have been excited by the RF pulse. Spatial encoding is done with gradients that induce a slight difference in the magnetic field over the object (30). Since the Larmor frequency is directly proportional to the field strength, a gradient in field strength also produces a gradient in precession frequencies. Because the precession frequency is no longer the same for all the spins they do not point in the same direction but form a pattern of spin phase that changes over time until they are re-aligned with the B_0 field. The measured signal intensity at a given time reflects how the spatial pattern of spin phase fits the tissue structures. If the spatial pattern fits the tissue structures well, the signal intensity will be strong, and if the pattern of spin phase does not fit the tissue structures the measured signal will be weak (31). Patterns in spin phase can be created with gradients applied simultaneously in spatial the *x*-, *y*- and *z*-directions.

3.1.3 From *k*-space to image

Magnetic resonance imaging is not based on sampling in the image directly, but rather it samples a spatial frequency map called *k*-space. Images can then be reconstructed from the *k*-space via an inverse Fourier transform. In the most common case, sampling of *k*-space is done in lines on a Cartesian grid. Figure 3.2 shows how the *k*-space in Cartesian imaging is related to information in the final image. The distance between two subsequent samples, Δk, determines the field-of-view in the image. The width of the sampled *k*-space, k_{max}, determines the resolution (pixel size) of the reconstructed image, since it represents the highest spatial frequency sampled and is therefore directly related to the smallest structures it is possible to distinguish.

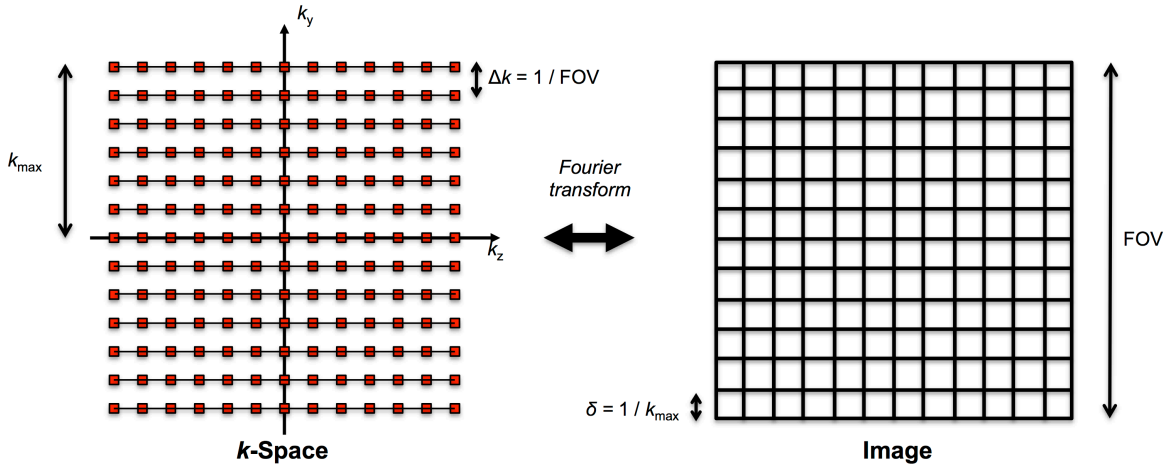

Figure 3.2 Relationship between *k*-space and image. The maximum distance in *k*-space, k_{max}, determines the resolution in the image with the pixel-size $\delta = 1 / k_{max}$. The sampling distance in *k*-space Δk, determines the field-of-view (FOV) = $1 / \Delta k$.

Naturally, the *k*-space does not have to be sampled using a Cartesian grid, nor is it limited to 2D imaging. A variety of different ways of traversing *k*-space exist, each with their own benefits and challenges. A 3D radial *k*-space trajectory was chosen in this work and is described in Section 3.4.

3.2 Cine imaging

The strength of MRI is to be found in the variety of trajectories and ways of capturing the NMR signal. In CMR this flexibility is used for flow measurements (32), T_1 and T_2 mapping (33,34), coronary angiography (35), and cine imaging (36). All of these provide a range of information about the structural and physiological condition of the heart. A central element is cine imaging that is used to visualize the mechanical function of the heart as well as measuring the volumes of the cardiac chambers. Already in the early 80's MRI started being used for cardiac purpose (37,38) and in 1986 cine imaging followed (36,39,40). Imaging the individual cardiac phases is done using the ECG, simultaneously measured from the patient, typically by segmented acquisition to ensure enough data in each cardiac phase (41).

3.2.1 Typical cardiac imaging slice orientations

In cardiac imaging, it is necessary to view the heart from different angles in order to visualize all structures of interest. Figure 3.3 shows an example of four views, which have been used in this work. Common for all these views is that the left ventricle is clearly visible. The short axis (SA) image is acquired perpendicular to the septum and is a cross-section of the left and right ventricles. The three long axis views are cutting the left ventricle through the apex and the base in different angles.

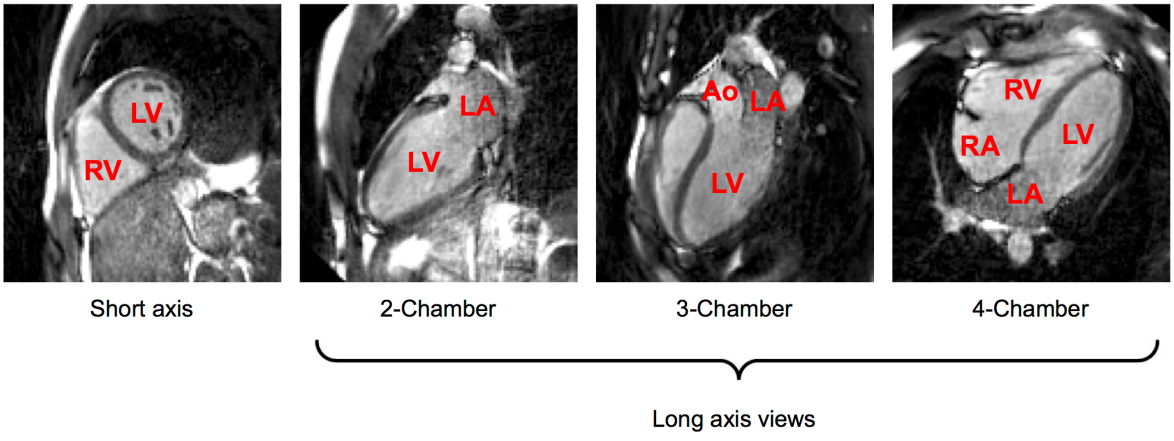

Figure 3.3 Typical cardiac image orientations. The short axis view is perpendicular to all the long axis views. Left ventricle (LV) is visible on all the images, left atrium (LA) on all the long axis images, and right atrium (RA), right ventricle (RV) and aorta (Ao) are all seen in at least one image angle.

Different cardiac views are necessary in cine imaging, not only to visualizing how the heart works, but because the images are used for measuring LV volumes. In standard cine imaging a stack of 2D SA cine image slices are acquired that covers the ventricles from apex to base. Commonly one or two images are acquired during a single breath hold. LV volumes in different cardiac phases can be segmented from the endocardial border in the SA images and the long axis images are used to ensure correct segmentation close to the apex and the base of the heart. Planning and positioning of each image position takes time, and if not done correctly might lead to difficulties in segmenting the ventricle. One of the advantages in 3D imaging is that only one acquisition that does not require much positioning is necessary. From a 3D whole-heart image volume, image planes through the heart can be retrospectively re-sampled in any angle and position.

3.3 Challenges with respiratory motion in cardiac imaging

Magnetic resonance imaging is a complex methodology and imaging the heart adds even more difficulties that require high precision and careful consideration. Most challenging is the constant motion from cardiac pumping and respiration (42). ECG and respiration are usually measured in patients undergoing a CMR exam. Cardiac motion is generally dealt with by using the ECG for triggering the acquisition of specific cardiac phases and requires no patient co-operation. Respiratory motion, however, is often dealt with by respiratory suspension by asking the patients to hold their breath.

Breath holding has the purpose of limiting respiratory motion of the heart, caused primarily by the diaphragm, while data is acquired. Breath holding is an integrated part of many clinical protocols, and pulse sequences are designed to enable a pause in acquisition to allow for breathing between acquisitions. Normal clinical CMR exams can require up to 50 breath holds and each breath hold is typically 10-15 seconds in duration. This means that the patients hold their breath for more than eight minutes in total during a 45- to 50-minute exam. Fatigue or inability to hold ones breath can contribute to reduced image quality and artifacts (43). Many patients experience difficulties performing breath holds sufficiently, and even in those that do not have difficulties, breath holding can pose problems when performed in varying diaphragm positions.

Motion artifacts from breathing appear differently depending on the *k*-space trajectory used. In Cartesian imaging, motion artifacts may appear as ghosting, where moving structures are displaced and appear in several different positions in the image (42). In many pulse sequences, respiratory motion artifacts might manifest as blurring and image distortion in the areas of motion (42). Figure 3.4 shows an example of Cartesian 2D SA images with a good breath hold compared to one with substantial respiratory motion. In the image with poor breath holding, both blurring and ghosting are present.

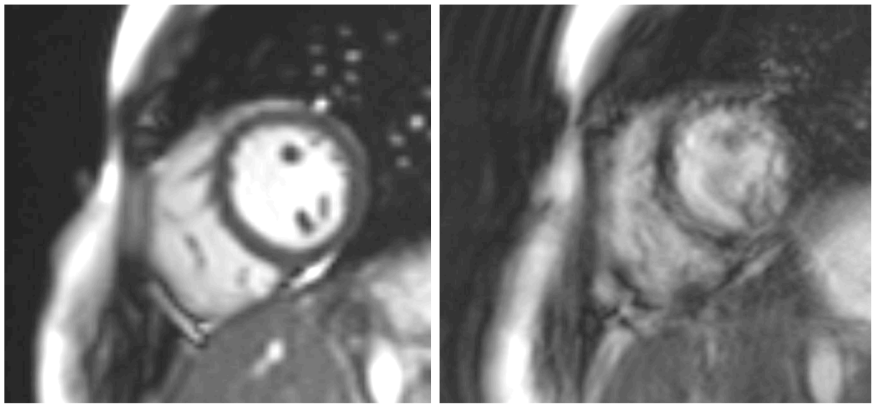

Figure 3.4 Poor breath holding effects. Left: short axis image with good breath hold. Right: the same image position, but acquired during a poor breath hold.

Cartesian acquisition trajectories tend to produce more coherent image artifacts. Motion artifacts from radial trajectories, on the other hand, are less coherent and appear blurrier, which in some cases makes them easier to read through (44). An example of images with and without breath holding for Cartesian compared to radial acquisition trajectories is illustrated in Figure 3.5 where the motion artifacts appear differently.

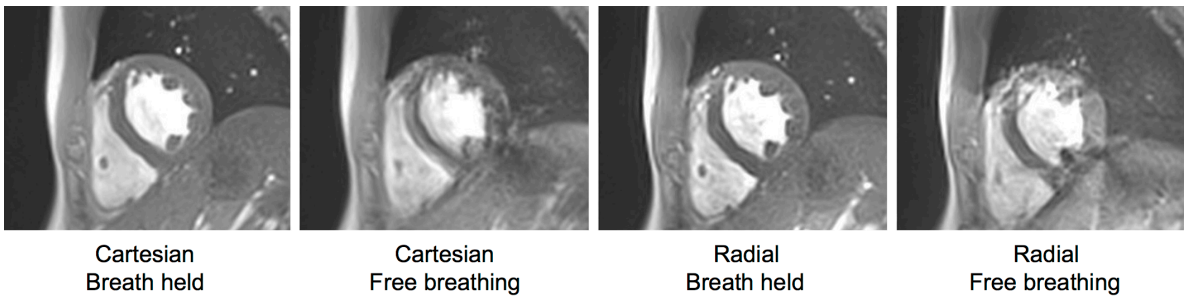

Figure 3.5 Radial vs. Cartesian and breathing vs. breath held. Radial and Cartesian images obtained during breath holding have similar image quality, but show different motion artifacts during breathing. *Images obtained and modified from* (45).

Varying diaphragm position (respiratory amplitude) from breath hold to breath hold can cause slice misalignment in stacks of 2D cine images when each image has been done at individual breath holds (35,46). Particularly, this is an issue when measuring LV volumes, and Figure 3.6 illustrates why. SA slice positions are shown on the 4-chamber image on the left and LV volume was segmented from the stack of SA slices. A long axis view of the segmented 3D LV endocardial border from the SA image stack is shown on the right. As can be seen in the 4-chamber image, the endocardial border runs smoothly along the blood pool, but the segmented chamber has an irregular and discontinuous shape because breath holding for individual image slices was done at different respiratory amplitudes. Since the heart rests directly on the diaphragm, this causes the heart to be at different positions inside the chest. Whole-heart imaging provides a solution to this problem.

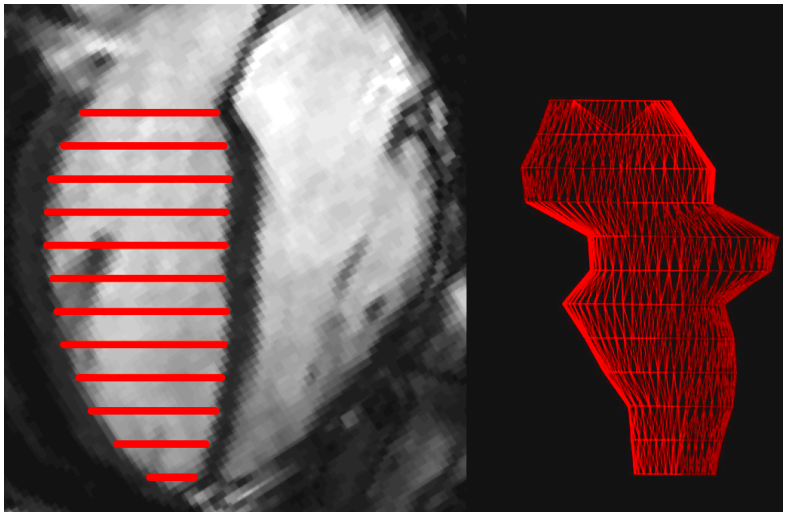

Figure 3.6 Effects of breath holding in different respiratory positions. Left: 4-chamber view with illustration of short axis image positions acquired in different breath holds. Right: volume of the segmented left ventricle from the stack of short axis images show misalignment of the images and faulty depicturing of the LV volume.

3.4 Trajectory design and sampling of *k*-space

Whole-heart free breathing cardiac imaging would eliminate the issue of slice misalignment and time consuming planning of multiple slice positions. 3D imaging would, furthermore, allow for multi-planar reformatting, which is a technique for generating arbitrary image slices from a 3D image volume. A particular patient group that would benefit from whole-heart imaging is patients with congenital heart disease because they have abnormal anatomy (47). In congenital heart disease patients, the clinicians would be able to get a more detailed understanding of the anatomy if they are given the ability to manipulate the view angle after acquisition.

3.4.1 Design choice

According to the design requirements presented in Section 1.2, the trajectory needed to perform well during free breathing and enable extraction of respiratory information. Section 4.1 provides a description of how the respiratory information was extracted from the data and why the measured bellows signals were not sufficient. The choice fell on a double golden-angle radial trajectory (48). Figure 3.7 shows an illustration of how the 3D *k*-space with this trajectory looks like.

Radial sampling was chosen partly because it is more robust to motion artifacts than Cartesian sampling (44), but mainly because radial acquisition samples the *k*-space center every few milliseconds. The center of *k*-space represents the lowest spatial frequencies found in the imaged object and thereby the largest structures. This is of importance in capturing motion since motion is simply movement of large structures. How the *k*-space center in radial sampling provides information about large structures is illustrated in

Figure 3.8. For simplicity Figure 3.8 is from a 2D acquisition, but the principle is the same in 3D. The top left part shows a radially sampled 2D *k*-space and below the SA image reconstructed from the radial *k*-space. On the right, only the center part of *k*-space is used for image reconstruction. In this case the image is extremely blurry and no details are seen. But the contour of the heart, lungs and other structures are easily visible, and it is these structures that move during respiration, which needs to be captured.

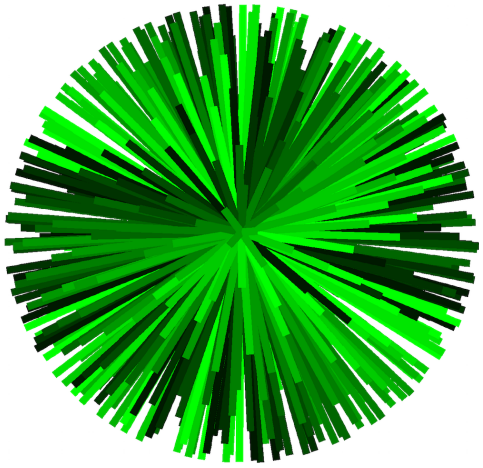

Figure 3.7 Radial double golden-angle 3D *k*-space.

Golden-angle ordering of radial spokes is increasingly used for free breathing CMR (49). Golden-angle acquisition was initially developed in 2D with every spoke being acquired at an angle increment of 111.25° compared to the previously acquired radial spoke (50). Calculation of the golden angle, θ, is based on the golden ratio, φ, by

$$\theta = \frac{180°}{\varphi} = \frac{180°}{(1+\sqrt{5})/2} \approx 111.25° \tag{5}$$

Golden-angle radial imaging has two important properties; first, it can run infinitely and always acquire a new radial *k*-space spoke that hasn't been sampled previously (see 2D golden-angle acquisition in Figure 3.9), and second, for any subset of consecutive spokes it provides relatively uniform *k*-space coverage. The ability to continuously acquire new data and cover large parts of *k*-space with a few spokes makes it particularly suitable for free running imaging as well as retrospectively sorting the data into different phase bins of the cardiac and respiratory cycles using a subset of the acquired spokes. The 3D double golden-angle radial trajectory has the same properties as the 2D trajectory, and the angle increments are calculated from two golden means derived from Fibonacci series, φ_1 and φ_2.

The type of trajectory chosen only says something about the order with which we sample *k*-space. Most of the contrast properties arise from combinations and timing of RF

pulses, gradients and readout moments, the so-called pulse sequences. In this work the pulse sequence used is balanced steady-state free precession (bSSFP), which is advantageous in cardiac imaging because it provides high contrast between the blood and myocardium and they are fast. An example of the pulse sequence for the double golden-angle radial trajectory combined with bSSFP readout is illustrated in Figure 3.10.

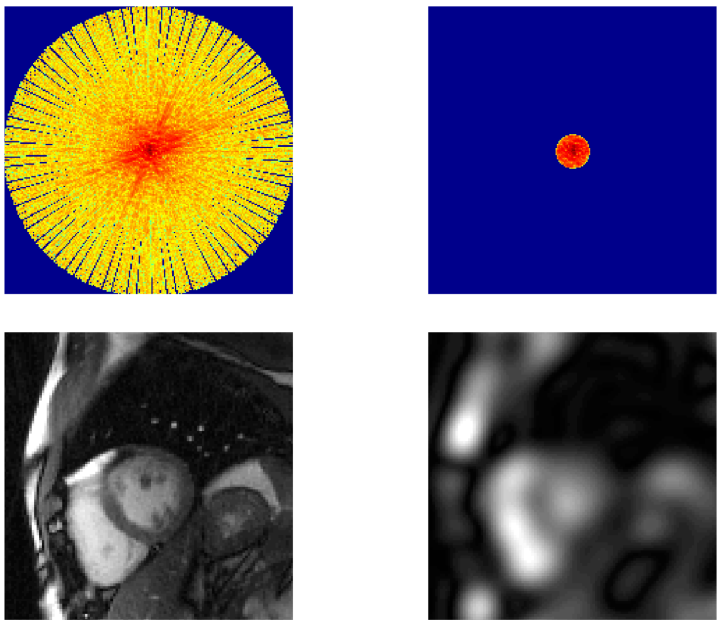

Figure 3.8 Motion information in *k*-space center. Top: 2D radial *k*-space. Bottom: Image reconstruction of the above *k*-space. Right: fully sampled *k*-space provides good resolution in the image. Left: image reconstruction of only the center of *k*-space yields an image with very low resolution, but clearly shows all the large structures that are moving.

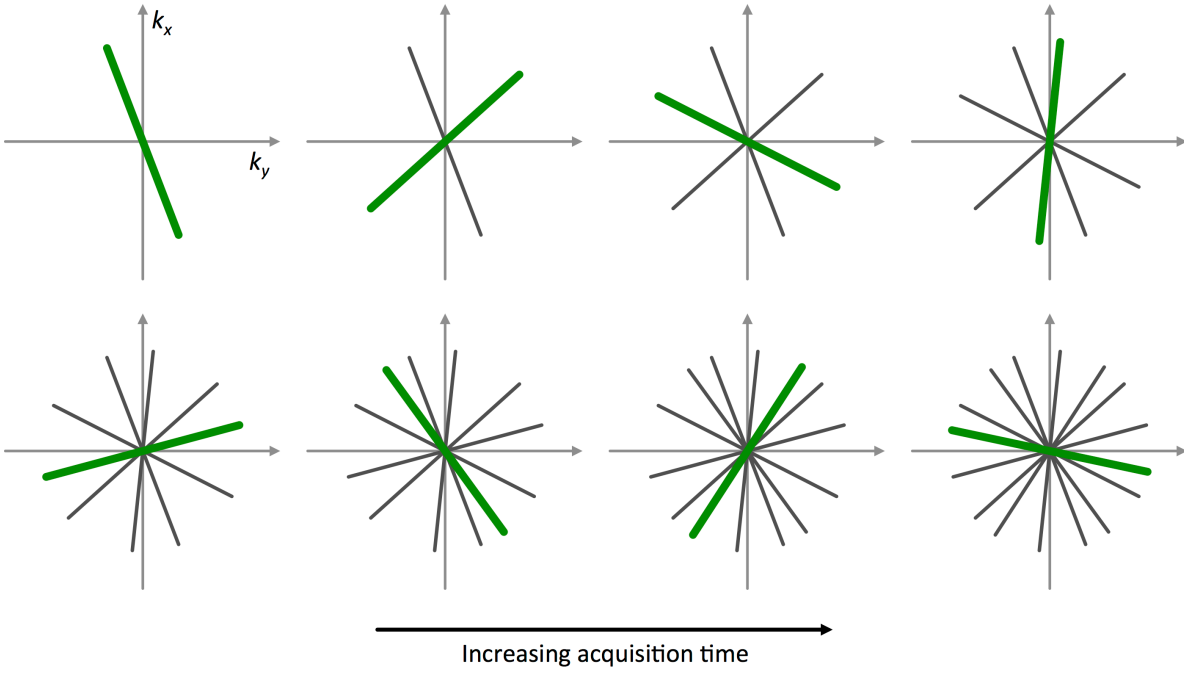

Figure 3.9 2D golden-angle sampling of *k*-space. From left to right a new radial spoke (green) is acquired. Every new spoke fills one of the largest gaps in *k*-space.

For each repetition time in the pulse sequence diagram one whole radial *k*-space spoke is acquired after RF excitation when the analog-to-digital converter (ADC) is switched on. The *x*-, *y*- and *z*-gradients are used to acquire *k*-space lines with different angles.

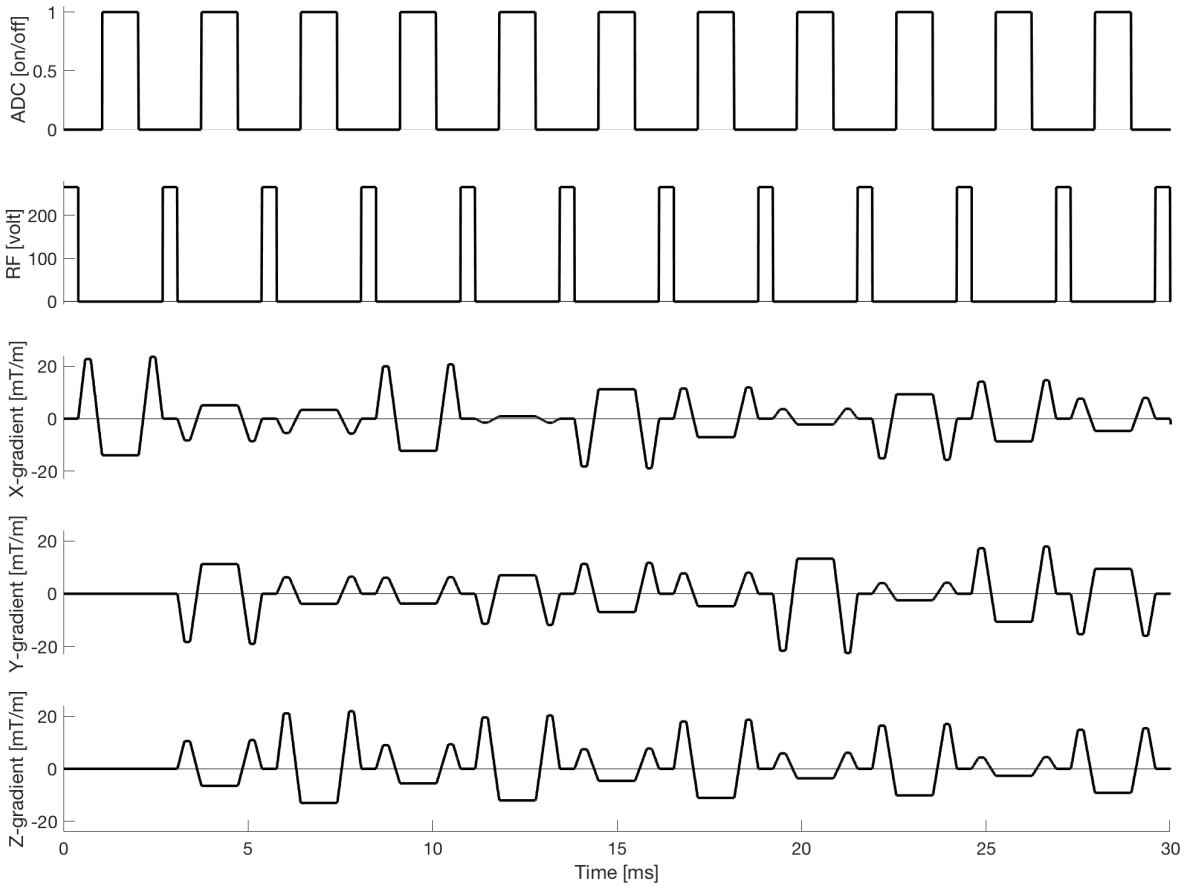

Figure 3.10 Pulse diagram for bSSFP 3D double golden-angle imaging.

3.4.2 Double golden-angle acquisition compared to other 3D radial trajectories

There are many ways of constructing a 3D radial trajectory. In the following we will take a look at the differences between some of the more common ones for cardiac free breathing imaging and how they differ from the double golden-angle trajectory used here.

But first, let's take a look at the most generic 3D radial trajectory. This is a Koosh ball trajectory, like the double golden-angle trajectory, that has a linear ordering of the acquired radial spokes. Figure 3.11 shows how each spoke end is positioned on the surface of the *k*-space trajectory sphere. Only the top half of the sphere is shown because each spoke goes through the center and ends on the opposite side of the sphere. Acquisition order of the radial spokes follows a simple spiral pattern from pole to the equator of the sphere. This trajectory is preset to acquire *k*-space data for one image volume and has a fixed scan time. Binning of the data afterwards using subsets of spokes is not possible since it would leave large gaps in *k*-space, resulting in streaking artifacts. It is for that reason also sensitive to motion and would not work well with free breathing.

Many 2D and 3D *k*-space trajectories are traversing *k*-space with similar small steps, making it unsuitable for data binning. There is therefore a need to rethink *k*-space sampling strategies.

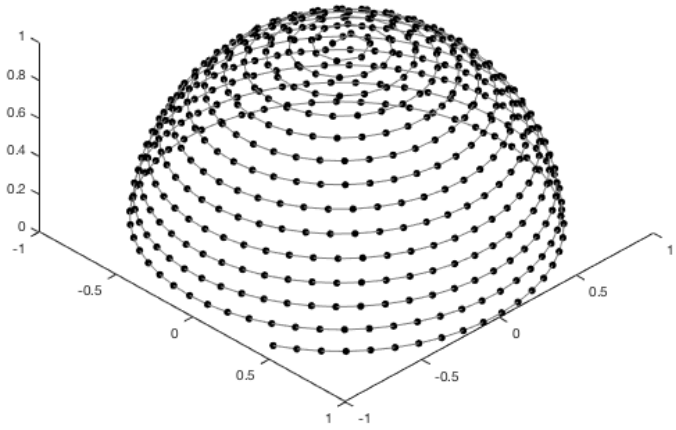

Figure 3.11 *k*-Space sampling of a 3D radial trajectory with linear spoke order. Each sample on the sphere surface represents the tip of one radial spoke. Only the top half of the trajectory sphere is shown because each spoke goes through the center of *k*-space and finished on the opposite side of the sphere.

A major advantage with the 3D linear radial trajectory, however, is the uniform *k*-space sampling that produces an image relatively free from streaking artifacts.

One way of ensuring a more uniformly sampled radial 3D *k*-space, but keeping the binning properties of golden angle, is with the spiral phyllotaxis trajectory shown in Figure 3.12 (51). In spiral phyllotaxis, the *k*-space spokes are acquired in small spirals from pole to equator, and each new spiral is rotated with a golden-angle compared to the previous.

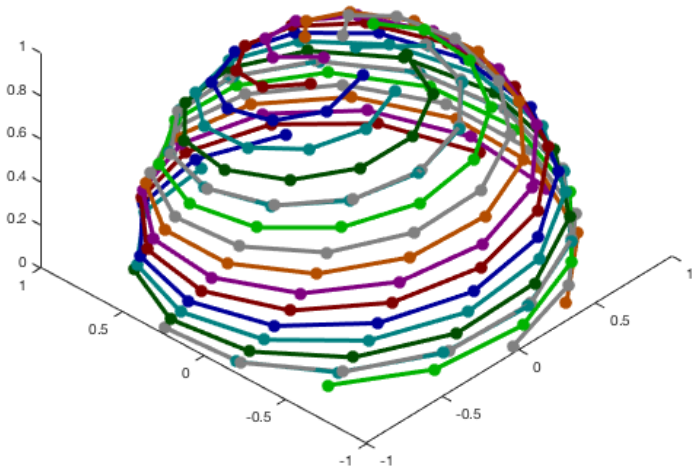

Figure 3.12 *k*-space sampling of the spiral phyllotaxis trajectory. Each sample on the sphere surface represents the tip of one radial spoke. Only the top half of the trajectory sphere is shown because each spoke goes through the center of *k*-space and finished on the opposite side of the sphere. Spokes are acquired in a spiral manner and each new spiral is rotated with the golden angle compared to previous spiral.

The spiral phyllotaxis requires a preset number of radial spokes to produce an evenly sampled *k*-space, where the double golden-angle trajectory can run for any amount of time and still produce a relatively even spoke distribution. In Study I, simulation of the spoke distribution on the spherical *k*-space surface after binning showed that the double golden-angle and spiral phyllotaxis performed similarly. The spiral phyllotaxis had a few large gaps in the binned *k*-space, but whether or not that has any noticeable impact on image quality is not clear.

A large advantage of the spiral phyllotaxis and linear 3D radial trajectories is the small angle increment from one acquired spoke to the next. This requires smaller *k*-space jumps and thereby less eddy currents are being induced in bSSFP imaging (52).

During the work of Studies I-II, it was realized that the double golden-angle trajectory produces substantial eddy current-related artifacts. To avoid this, an extension to the derivation of the two golden means was used to design tiny double golden-angle trajectories with smaller angle increments between consecutive spokes. The mean angle between consecutive spokes was reduced from 94° to 7° while keeping the ability for free-running acquisition and binning properties. An example of how this improved image quality can be seen in Figure 3.13 for phantoms and in Figure 3.14 for a healthy volunteer. The tiny double golden-angle trajectory clearly reduced eddy current related artifacts without decreasing the *k*-space uniformity after binning.

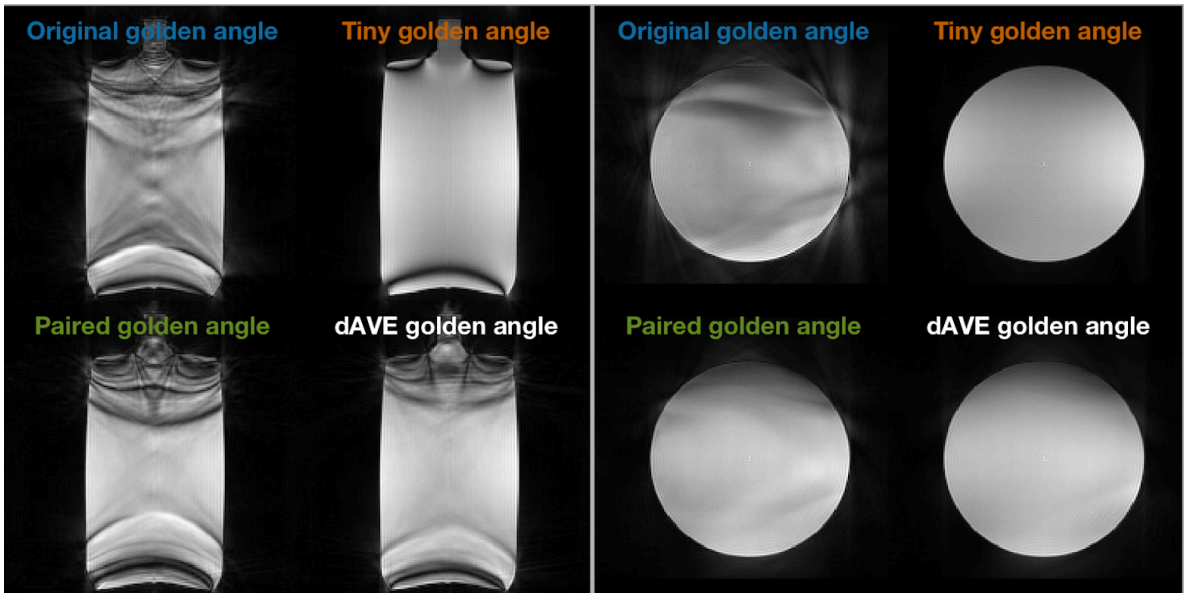

Figure 3.13 Eddy current effects with different types of double golden-angle trajectories in phantoms. The tiny double golden-angle was found to produce the most uniform images.

To reduce eddy currents in bSSFP imaging a double averaging (dAVE) technique has previously been suggested by acquiring the same *k*-space line twice to average out the off-resonance effects produced within two repetitions (53). Therefore, the dAVE

technique was tested as well as a paired hybrid scheme where every second line in the trajectory followed the original double golden-angle method and every second was a tiny angle increment to the previous line. The dAVE technique has theoretically been considered the optimal solution and was expected to perform better than any of the other three trajectories, but it was found that the tiny double golden-angle trajectory performed best, which could suggest the existence of long-lived eddy currents that is not accounted for by the dAVE technique.

Koosh-ball trajectories, such as the spiral phyllotaxis, original- and tiny double golden-angle trajectories all sample the center of *k*-space for every repetition time. This is good for capturing the motion, but a downside is that it severely oversamples the center of *k*-space compared to the edges, and might therefore be a relatively inefficient way for 3D *k*-space sampling.

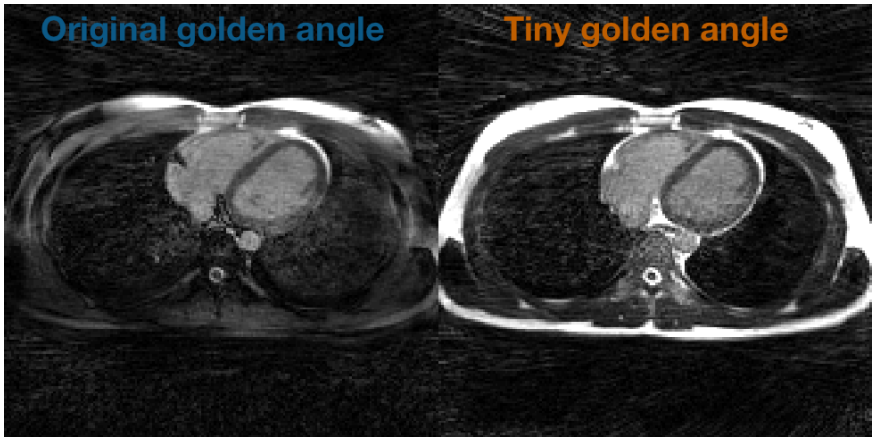

Figure 3.14 Eddy current effects with different types of double golden-angle trajectories in a healthy volunteer. The tiny double golden-angle trajectory reduces the off-resonance effects seen by signal cancellations in the fat with the original trajectory.

A way to overcome the inefficient oversampling has been suggested with a golden-angle radial stack-of-stars trajectory (Figure 3.15) which possesses a combination of radial and Cartesian properties (54). It has radial properties in two dimensions and Cartesian in the third dimension where sampling is uniform and more efficient. Advantages of the Cartesian dimension are that it allows for partial Fourier (55) and other Cartesian tricks for speeding up the acquisition. However, the stack-of-stars is often used for acquisition of image volumes without isotropic voxels causing the planned image volume to depend on orientation, thus making the acquisition more complicated. It is possible to acquire isotropic voxels with the stack-of-stars, just not very common.

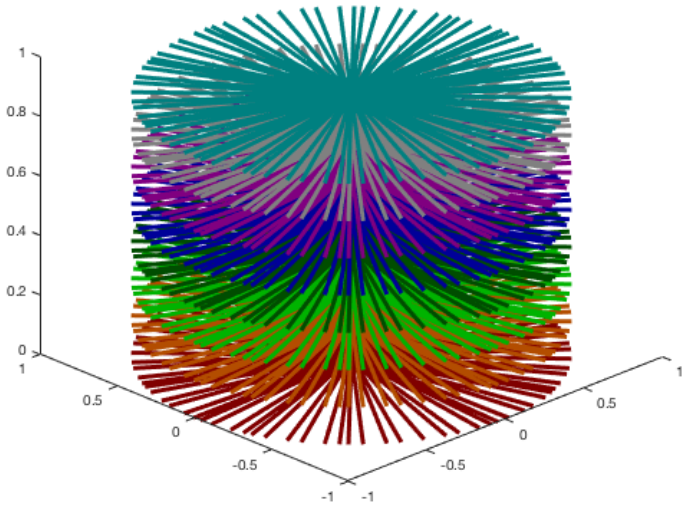

Figure 3.15 *k*-space sampling of the stack-of-stars trajectory. Stack-of-starts acquisition of a 3D image volume combines Cartesian properties in one dimension with 2D golden-angle radial.

3.5 Image reconstruction

A major drawback to non-Cartesian *k*-space sampling involves a more complicated and time-consuming image reconstruction process. Non-Cartesian data, including radial sampling, requires a gridding operation to a Cartesian grid during the image reconstruction process in where the non-Cartesian data points are being resampled to a Cartesian grid (56). This is both a time-consuming operation and leads to smoothing in *k*-space from interpolation. However, this is a necessary trade-off to have the advantages of non-Cartesian imaging. The gridding process is combined with a Fourier transform during image reconstruction and is therefore often referred to just as a non-uniform fast Fourier transform (NUFFT) (57,58). It is due to the fast Fourier transform algorithm that a Cartesian grid is required.

In 3D imaging, the amount of data necessary for fully sampling a *k*-space volume for several bins representing different cardiac or respiratory phases using a Koosh-ball trajectory would require hours of scan time. Therefore, undersampling strategies can be used where the missing data is synthesized retrospectively in the image reconstruction processes. Parallel imaging is a technique where spatial sensitivity information in each receiving coil element is used to regain the missing data points. The acquisition time was substantially reduced in Study II by implementation of an iterative non-Cartesian parallel image reconstruction called conjugate gradient sensitivity encoding (cgSENSE) (59).

Chapter 4

Cardiac Imaging in the Cardio-Respiratory Space

Robust methods for visualizing and measuring the cardio-respiratory variation in cardiac dimensions are necessary for diagnostic purposes, and it is therefore crucial to obtain precise information about the cardiac and respiratory phases at a given time point. The cardiac and respiratory cycles form a 2D temporal map of cardiac and respiratory phase and provide the basis for imaging the LV dimensions in the cardio-respiratory space. In this work, cardiac phase information was extracted from the ECG and respiratory phase information from *k*-space data in form of respiratory self-gating signals, which are described in Section 4.1. The 2D cardio-respiratory phase map is presented in Section 4.2 and results of respiratory variation in LV dimensions are summarized in Section 4.3.

4.1 Respiratory self-gating

Several different ways of measuring respiratory motion exist. As a standard part of the CMR exam, respiratory motion is measured with bellows, which indirectly measures respiratory movement from a pressure transducer strapped to the upper abdomen. When the patient inhales, the pressure under the transducer strap increases and is registered in the transducer, and when the patient exhales, the pressure under the strap decreases. The first examples of free breathing cardiac imaging were done with bellows signals by prospectively gating the data acquisition in a predefined window of the respiratory cycle, typically during end expiration (60). Though improvements have been made in prospective gating with respiratory bellows (61), it still suffers from only providing an indirect measure of the diaphragm position during respiration (42,61,62).

Normal breathing patterns can vary quickly in frequency and amplitude, and ideally, a respiratory gating-signal needs to account for this. In Figure 4.1, a respiratory bellows signal from a healthy volunteer illustrates some of the aspects a gating-signal needs to

account for. Both the frequency and amplitude visibly changes several times during the only 80 seconds displayed. Additionally, the form of each respiratory cycle differs over time. The larger circle marks a pause in end expiration, which is a normal occurrence in respiration. Changes in respiratory pattern (amplitude, frequency and form) happen quickly and a good respiratory gating method therefore needs to have the ability to measure the respiration more directly than the bellows.

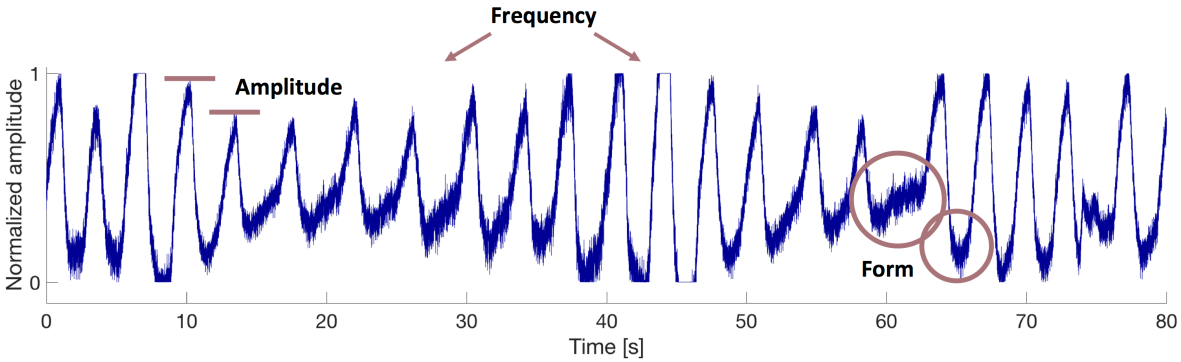

Figure 4.1 Respiratory bellows signal from healthy individual. Features of an ideal respiratory self-gating needs to account for varying amplitude and frequency (horizontal bars and arrows), accounting for changing form of the cycles (circles) as well as detecting abnormal instances in the respiration (e.g. the occurrence after 75 seconds).

Respiratory navigators (NAV) are examples of a more direct measure of respiration done with MRI scanners (63). NAV signals typically come from pencil beam acquisitions, positioned perpendicular to the diaphragm. After a 1D Fourier transformation of the *k*-space lines, they provide a projection view through the thoracic cavity and, when acquired over time, a motion-mode (M-mode) view of the diaphragm position. They are typically acquired in a rate of 1-3 acquisitions per second and the diaphragm position is extracted by cross-correlation between the lines in the M-mode view (64). It has been shown that NAV provides more efficient prospective gating than respiratory bellows and resulted in images less affected by motion blurring (61,62), but they can also be used for retrospective gating. NAV signals are still frequently used, though they offer a rather low temporal resolution and have to be manually positioned.

Prospective respiratory gating of data acquisition has the disadvantage that the acceptance window for data acquisition is determined by previous respiratory cycles, and not the cycle data is in fact acquired in. If respiratory frequency or amplitude changes, data would be acquired during the wrong respiratory phase and would either lead to motion artifacts or prolonged scan time if the data is rejected. Retrospective gating, on the other hand, allows for data to be correctly sorted according to respiratory phase and can be redone if the images show motion artifacts and thereby offers much more flexibility.

Retrospective gating was used in Studies I-IV, and in Studies I-III and the gating signal was extracted from the center of each acquired radial spoke using the low spatial resolution in the *k*-space center, thus providing a temporal resolution of a few milliseconds. A 1D *k*-space center signal was combined from information in each coil-element and band-pass filtered to isolate the respiration frequencies. Because the respiratory gating signal was extracted from the data itself, the data was essentially self-gated.

The *k*-space based respiratory self-gating signal did have some issues and was replaced in Study IV. The main problem was that it only contained phase information about the respiration and was therefore suspected of not sorting the data correctly.

Therefore, a projection-based self-gating, similar to the NAV technique, was implemented into the double golden-angle radial trajectory. The projection information came from a superior-inferior radial spoke inserted into the trajectory for every 25th spoke and thereby had a temporal resolution of 64 ms, 5-10 times more than NAV. The diaphragm position was extracted using principal-component analysis and coil clustering (65).

The *k*-space based self-gating signal failed in patients. Figure 4.2 shows an example of respiratory self-gating signals using projections and *k*-space center from one patient, and the superior-inferior projections are illustrated as an M-mode view in the top of the figure. Three important aspects of respiratory self-gating can be seen in Figure 4.2; first, the *k*-space based signal completely disregards the amplitude of the respiration where the projection-based has both phase and amplitude. Second, the *k*-space based signal does not follow the bellows signal very well, which may be the reason it failed in patients. And third, there is a phase shift between the projection based signal and the bellows signal which likely illustrates the finding in (61,62) that NAV (also a projection based method) provided images with less motion blurring than bellows.

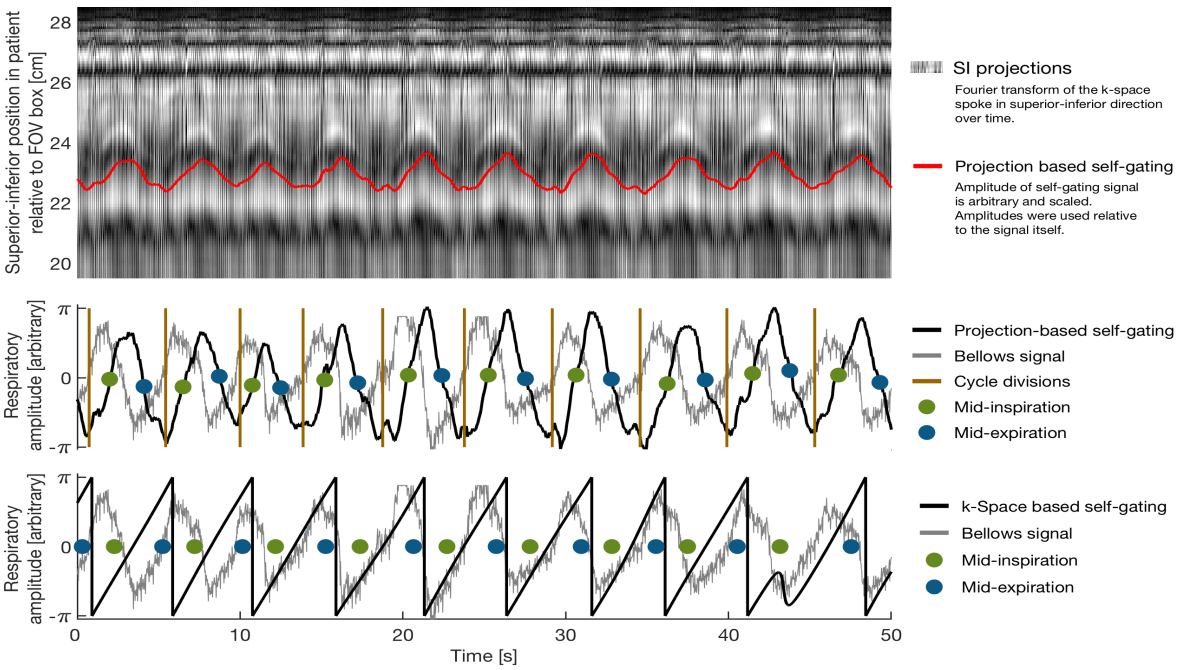

Figure 4.2 Examples of self-gating signals from projection based (middle) and *k*-space based (bottom) methods. The superior-inferior (SI) projections are shown in the top graph with the extracted self-gating signal superimposed. Note how the *k*-space based method fails to follow the respiratory bellows signal and at the same time do not account for changes in amplitude.

4.2 The cardio-respiratory phase map

Imaging the heart in 5D comprises three spatial dimensions together with the two cardiac and respiratory motion dimensions. The cardio-respiratory map is illustrated in Figure 4.3 and describes a 2D combination of cardiac phase and respiratory phase. Cardiac phase is measured in percent from one R wave to the next and respiratory phase in percent from mid expiration to the next mid expiration, where the intra-thoracic pressure is highest.

The cardio-respiratory phase map is cyclic and can be divided into an endless combination of cardiac and respiratory bins. In the example in Figure 4.3 (left) the whole cardiac cycle is divided into 25 bins and isolated to respiratory end expiration (design in Study I). Each green box illustrates the data that has been acquired in this particular combination of cardiac and respiratory phase, i.e. what is imaged with a conventional breath held cine. Figure 4.3 (right) illustrates the flexibility of free breathing acquisition where the entire respiratory cycle is divided into 8 bins and isolated to the diastasis part of diastole (design in Study II). Any combination of cardiac and respiratory phases can be made.

The bin sizes are limited by the amount of data that has been acquired, as each image volume is reconstructed from the data being sorted into each bin. A decrease in bin size improves the temporal resolution, but each image volume will comprise less data. The bin sizes therefore have to be designed as a trade-off between scan time, amount of data and

temporal resolution. An increase in scan time will result in more data that can either be used to improve the image quality or the cardiac or respiratory temporal resolution, or both. On the other hand, a decrease in scan time is possible with maintained image quality with the expense of temporal resolution.

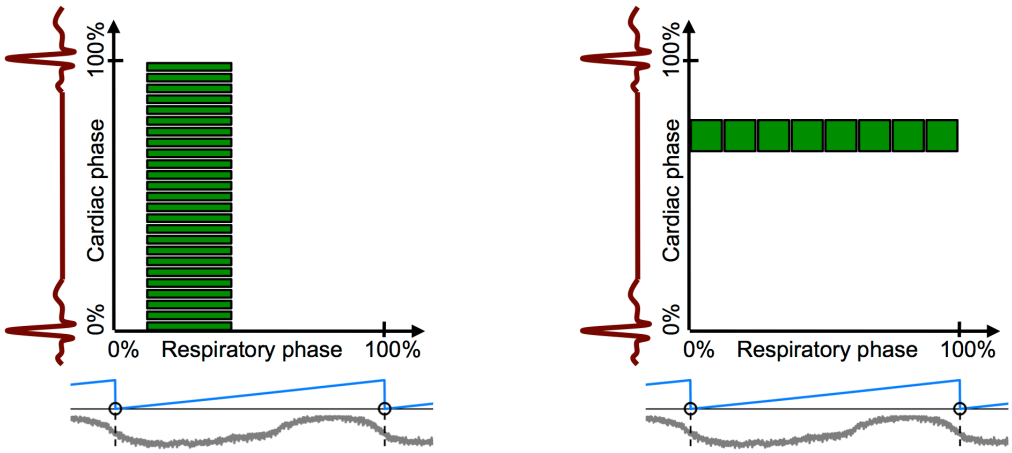

Figure 4.3 Illustration of the cardio-respiratory phase maps. The cycling cardiac and respiratory phase can be divided into any combination. Each green square represents the data binned into this phase combination from which an image volume is reconstructed. Left: example of 25 cardiac bins in end expiration. Right: example of 8 respiratory bins in the diastasis phase of diastole.

Tailoring the data acquisition to a given cardio-respiratory phase map, whether for displaying cardiac function or measuring ventricular volumes during respiration, only ensures an average amount of data in each bin. This leaves a margin for data to be discarded if acquired during irregular respiratory cycles or cardiac arrhythmia. The amount of data may vary because the occurrence of any combination of cardiac and respiratory phases might happen more or less frequent during the acquisition. The precise amount of data therefore varies from bin to bin, and from experience often displays a pattern dependent on the number of cardiac cycles per respiratory cycle, as well as the heart rate and respiratory frequency of the subject. Figure 4.4 shows an example of a cardio-respiratory phase map divided into 25 cardiac phases and 10 respiratory phases and a diagonal pattern is visible from top left to bottom right. This particular cardio-respiratory phase map is constructed from a 40 minute long 3D double golden-angle radial acquisition. The amount of spokes per bin varies between 2,900 and 4,600.

In unfortunate situations where there is a whole number of cardiac cycles per respiratory cycle, the variation could be much bigger. Thus, free breathing imaging in the cardio-respiratory space has some physiological uncertainties.

An advantage to retrospective self-gating and binning, however, is the ability to retrospectively change the bin size. Varying the bin size or shape within one temporal

image series would be of interest for a cardiac cycle where images in end diastole can be reconstructed from wider bins than in systole where cardiac movement is more rapid and more narrow bins would provide higher temporal resolution. In such a case, the images from end diastole could either have the same width of respiratory phase as in systole, or the respiratory bin size could be decreased, resulting in a similar image quality with higher temporal resolution in the respiratory phases. Retrospective stretching of bin sizes could accommodate many clinical questions and solve issues, which are yet unforeseen.

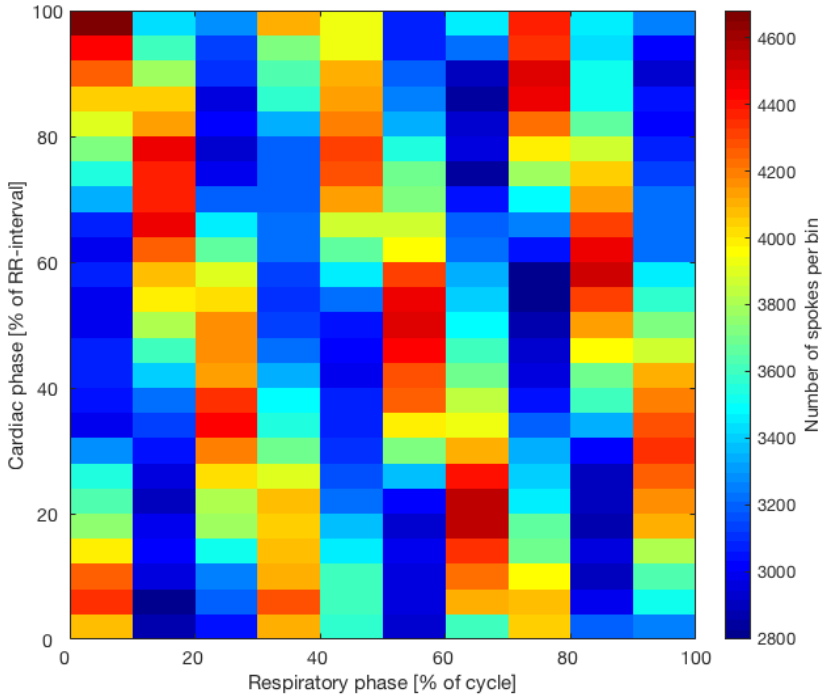

Figure 4.4 Cardio-respiratory phase map of 10 respiratory bins by 25 cardiac bins from a double golden-angle radial acquisition. Different colors represent the amount of radial spokes that have been binned into each phase combination.

Retrospective data binning could also be used to perform multiple reconstructions for both high cardiac and respiratory temporal resolution, without extra data acquisitions. Resolving the cardiac cycle typically requires 25 bins, and to get sufficient image quality one might require 25 % respiratory gating efficiency. 25 % of the respiratory phases would only give 4 respiratory bins, which is not enough for resolving the respiratory cycle. In that case, the data could simply be re-binned into a new design with 8 respiratory bins and wide cardiac bins in end diastole. This was done in Studies I and II, in which the same data was reused.

Overall, free running and free breathing 3D acquisition with retrospective binning the 2D cardio-respiratory phase map offers great flexibility and endless possibilities of imaging the whole heart in different cardiac and respiratory phases.

4.3 Results of cardiac imaging in the cardio-respiratory space

4.3.1 Initial two dimensional imaging

The resulting method for measuring respiratory variation in LV end-diastolic dimensions was a 3D whole-heart acquisition, but initial tests were done with a free breathing 2D golden-angle radial trajectory (50).

Free breathing continuous 2D golden-angle radial acquisition in a mid-ventricular SA slice was used to test the cardio-respiratory phase map and measure the respiratory variation in LV end-diastolic area. Self-gating in 2D was done from images reconstructed in a sliding-window manner. Both cardiac and respiratory self-gating was done in 2D from band-pass filtering and smoothing time signals created from the sum of image intensities. Figure 4.5 shows an example of a cardiac self-gating signal compared to the measured ECG. The signal nicely followes the ECG, but there were small shifts in the peaks compared to the R-peak in the ECG. This led to the decision of only focusing on respiratory self-gating since the bellows signal is much less reliable than the ECG.

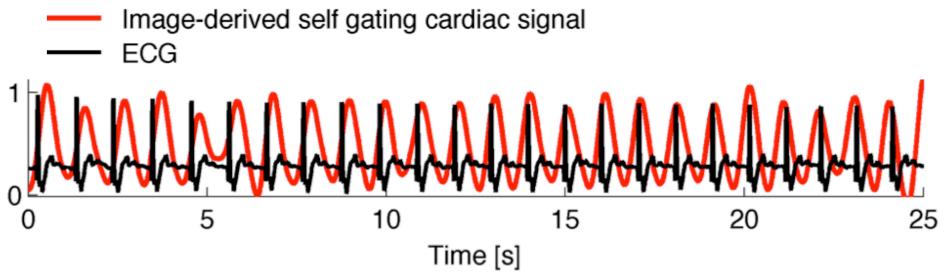

Figure 4.5 Example of a cardiac self-gating signal from 2D golden-angle acquisition. The signal was extracted by summing the image intensities from images series reconstructed in a sliding-window manner.

Cardiac self-gating is ultimately a desire for cardiac imaging, but clinical utility requires that it is at least equally as consistent and reliable as the ECG. Measuring the ECG in an MRI scanner is challenging because the gradient switching induces currents in the ECG leads, which decrease the quality of the ECG signal. Furthermore, ECG provides a measure of the electrical currents in the myocardium and is therefore only an indirect measure of the movements. However, the ECG's correlation to cardiac movement is so well studied and an accepted gold standard that it still is the best existing method for cardiac gating.

The LV area was measured from data binned into a cardio-respiratory phase map divided into 10 respiratory bins and 25 cardiac bins and images were reconstructed for the whole respiratory cycle in end diastole. Figure 4.6 shows an example of images from mid expiration and mid inspiration with the highest and lowest respiratory pressures, respectively. There is a clear difference in size and shape of the segmented LV endocardial border between these two phases.

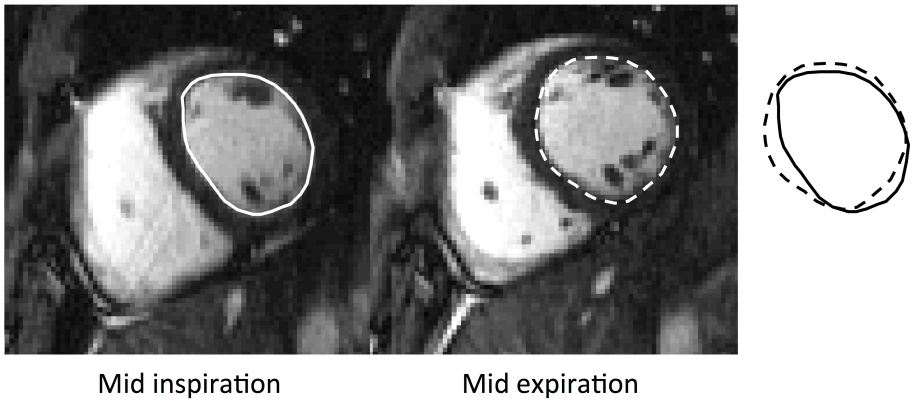

Figure 4.6 Respiratory-induced variation in LV end-diastolic area from 2D golden-angle acquisition in a healthy volunteer. Left: minimum LV end-diastolic area in mid inspiration. Middle: maximum LV end-diastolic area in mid expiration. Right: superimposed segmentations.

The LV area was measured in 8 healthy volunteers and the respiratory variation in LV area for the whole respiratory cycle is shown in Figure 4.7 and was approximately 9 % with respect to the mean area over the entire respiratory cycle.

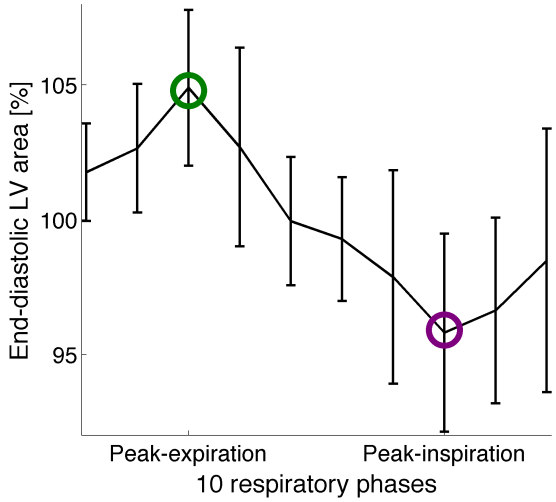

Figure 4.7 Respiratory-induced variation in LV end-diastolic area for 10 respiratory phases. Data points are mean ± standard deviation for 8 healthy volunteers. 100 % indicates the average of all volunteers.

Another way of visualizing the septal movement during respiration can be done with M-mode images, a method adapted from echocardiography. M-mode images are 1D projections through an image slice shown over time (see Figure 4.8). In these images the outer border of the left and right ventricles are not changing much during respiration, but the septal position matches the respiratory pressure variations.

Some of the advantages encountered with 2D compared to 3D imaging were higher image quality, shorter acquisition times and faster reconstruction times.

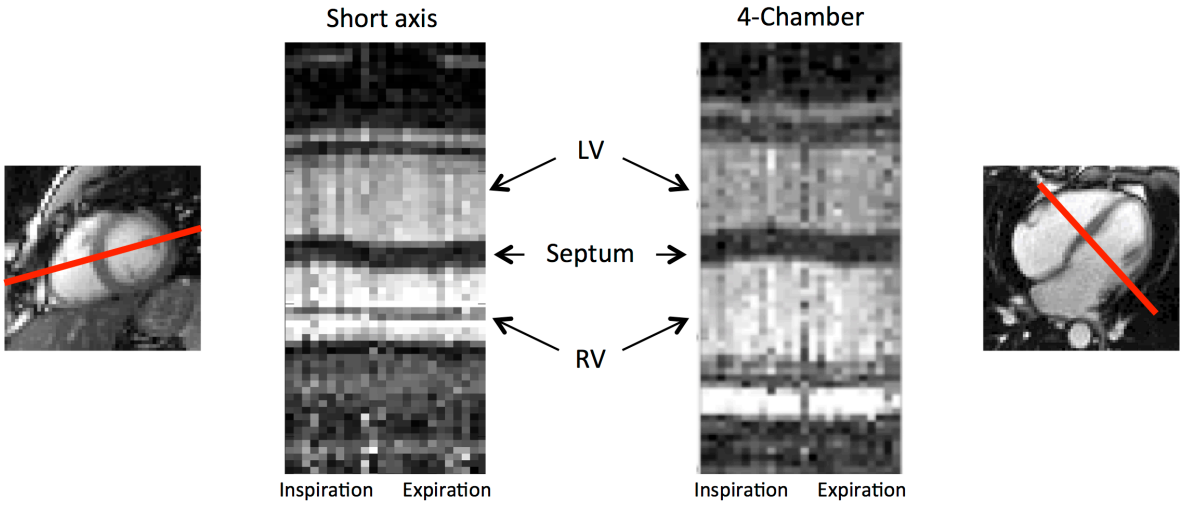

Figure 4.8 M-mode images showing septal movement during respiration from 2D golden-angle radial imaging. Left: a profile in a short axis image perpendicular to the septum has been extracted in end diastole for respiratory phases covering the entire cycle. Right: a profile in a 4-chamber image perpendicular to the septum has been extracted in end diastole for respiratory phases covering the entire cycle.

4.3.2 Results from 3D cardio-respiratory imaging

In Study I, the whole-heart free breathing double golden-angle radial acquisition was binned into 25 cardiac phases in end expiration and resolved over the entire cardiac cycle. Left ventricular EF, SV, EDV and ESV were measured in end expiration with the 3D free breathing technique and with a standard breath held 2D cine stacks of SA images. The main results can be seen in Table 1 and no difference was found between the two methods. Images comparing the 3D free breathing cine and 2D breath held cine techniques are shown in Figure 4.9.

Table 1 Comparison in measurements of left ventricular EF, SV, EDV and ESV between 3D free breathing and 2D breath held cine imaging. Measurements are from Study I.

	3D free breathing	**2D breath held**	**Difference**	***P*-value**
LVEF	59 ± 1 %	61 ± 5 %	1 ± 5 %	0.36
LVSV	107 ± 21 ml	113 ± 23 ml	6 ± 15 ml	0.50
LVEDV	183 ± 42 ml	188 ± 40 ml	5 ± 10 ml	0.43
LVESV	76 ± 22 ml	75 ± 21 ml	1 ± 9 ml	1.00

The main conclusion in Study I was that with free breathing 3D double golden-angle radial acquisition, the LV volumes during the cardiac cycle were comparable to the standard 2D breath held acquisition. In terms of image quality, the 3D free breathing method was found to be inferior to the standard breath held cine. Acquisition time for the free breathing 3D cine was 40 minutes compared to approximately 15 minutes for the 2D breath held cine, when accounting for the planning and additional acquisition of long axis views necessary for segmentation.

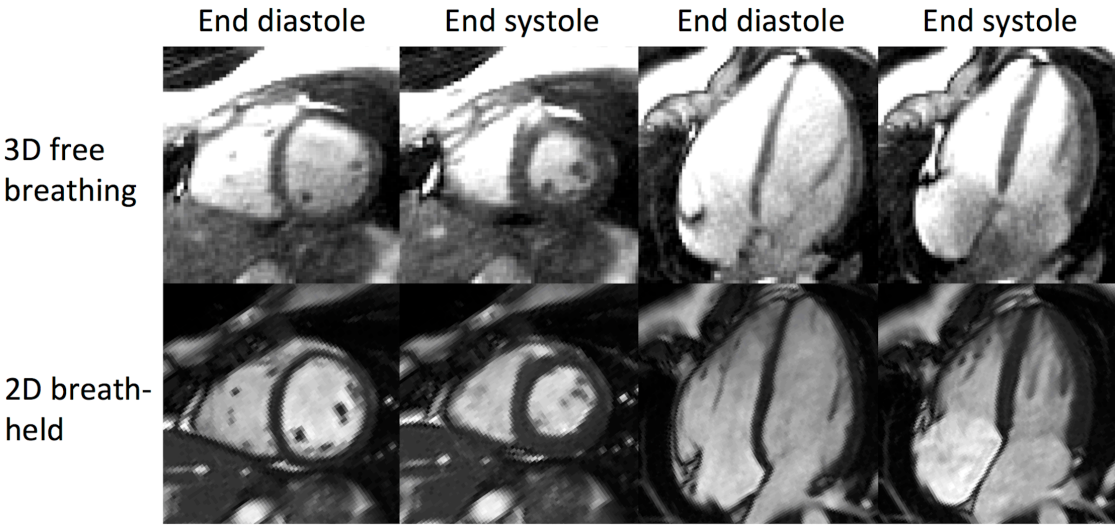

Figure 4.9 Images from free breathing 3D cine imaging compared to breath held 2D cine imaging.

Respiratory resolved LVEDV was investigated in Study II in healthy volunteers. Images comparing LV segmentation in mid inspiration and mid expiration are shown in Figure 4.10. For respiratory resolved imaging the cardio-respiratory phase map was divided into 8 respiratory bins covering the whole respiratory cycle, and one cardiac bin of 12.5 % of the cardiac cycle in the diastasis phase of diastole. Image acquisition could be reduced to 25 minutes because of the addition of the cgSENSE-algorithm to the image reconstruction. Also 9- and 4.5-minute acquisitions were tested and all three acquisitions durations were able to produce sufficient image quality for LV segmentation. Figure 4.11 shows the results of respiratory-induced variation in LVEDV for the three acquisition durations.

The respiratory-induced variation in LVEDV compared to maximum LVEDV in mid expiration was 5.9±0.3 % for 4.5 minutes, 5.3±0.4 % for 9 minutes and 5.0±0.4 % for 25 minutes of acquisition. No difference was found in LVEDV between the acquisition durations.

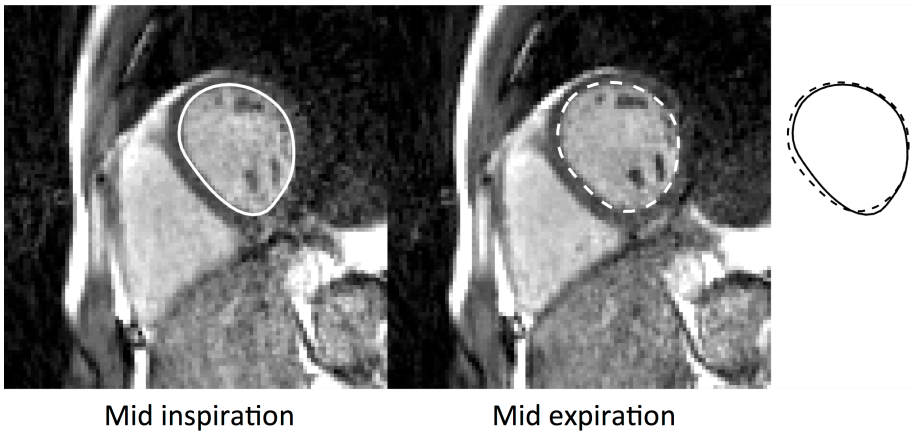

Figure 4.10 Respiratory-induced variation in LVEDV from 3D double golden-angle acquisition in a healthy volunteer. Left: minimum LVEDV in mid inspiration. Middle: maximum LVEDV in mid expiration. Right: superimposed segmentations. Images are from a 25-minute acquisition.

Also, the LV end-diastolic diameter in the septal-lateral direction and the anterior-inferior direction was measured from the 25-minute acquisition and the respiratory-induced variation in septal-lateral diameter was 8±0.4 % and in anterior-inferior diameter was 0.5±0.4 %. This confirms that the majority of change in LVEDV during respiration occurs in the septal-lateral direction.

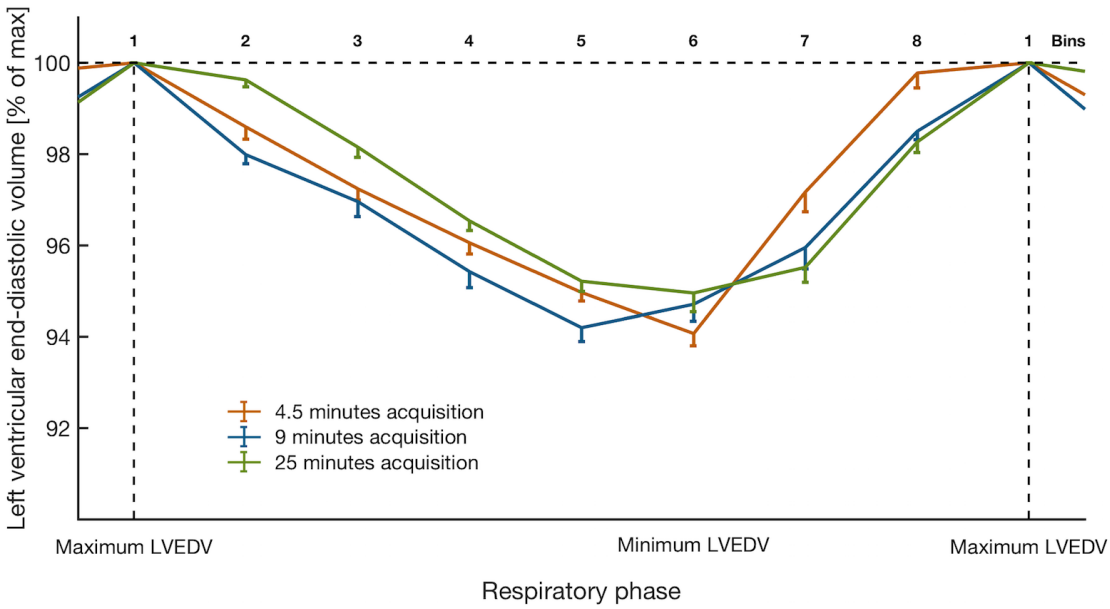

Figure 4.11 Respiratory-induced variation in LVEDV for 8 respiratory phases. 100 % indicates maximum expiratory LVEDV. Data points are mean ± standard error of the mean for 8 healthy volunteers.

Finally, the tiny double golden-angle radial acquisition with a superior-inferior projection based respiratory self-gating was used for imaging patients referred for varying clinical issues. Two bins were defined on the cardio-respiratory phase map, one of 15 % mid

inspiration and one of 15 % mid expiration. Both bins were 12.5 % of the cardiac cycle in the diastasis part of diastole. Differences between mid inspiration and mid expiration are shown in Figure 4.12. Acquisition duration in patients was 10.5 minutes and the respiratory-induced variation in LVEDV was 8±2 % compared to maximum LVEDV in mid expiration with the projection based self-gating. Also the original *k*-space based respiratory self-gating method was tested, where only 1±8 % difference was found in LVEDV. The conclusion was that the *k*-space based self-gating was not robust enough to capture the breadth of respiratory variations encountered in patients.

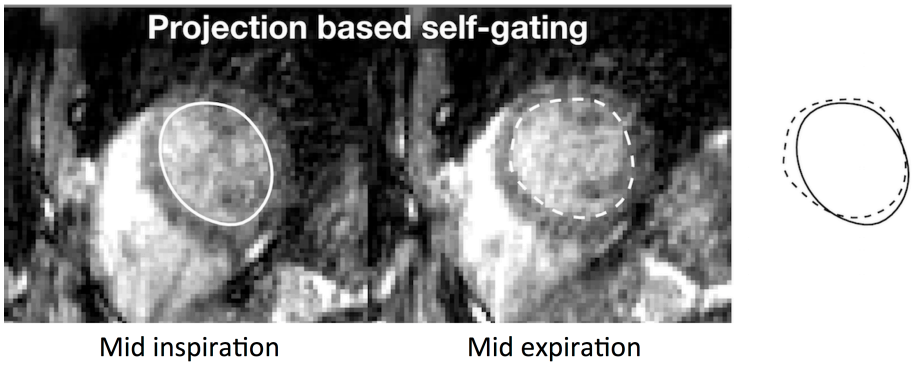

Figure 4.12 Respiratory-induced variation in LVEDV from 3D tiny double golden-angle acquisition in a patient. Left: minimum LVEDV in mid inspiration. Middle: maximum LVEDV in mid expiration. Right: superimposed segmentations. Images are from a 10-minute acquisition.

Chapter 5
Discussion

Respiratory variations in cardiac dimensions have been measured by left ventricular EDV, area and diameter. All these measures showed a respiratory-induced variation between 5 and 10 %. But what do these results actually mean? The results from cardiac imaging in the cardio-respiratory space will be discussed in a broader perspective in Section 5.1 and Section 5.2 looks at the difficulties with this method in transitioning from healthy volunteers to patients. Specific limitations are discussed in Section 5.3, and the author's view on the future for cardiac multidimensional cine imaging is presented in Section 5.4.

5.1 Cardiac imaging in the cardio-respiratory space

Respiratory-induced variation in LVEDV has, to my knowledge, only been investigated in one other study and was reported to be 6 % (66). Though this was only in one healthy volunteer, it is corroborating the findings herein that respiratory variation in LVEDV was 5-6 % in healthy volunteers. Other findings of respiratory variation in cardiac dimensions, including LV area and diameter, have been reported (16,17,67–69) and corroborate the findings in this work.

Study II showed no statistically significant difference in respiratory variation in LVEDV between 4.5-, 9- and 25-minute acquisitions, but there seemed to be a tendency for a slight decrease in LVEDV variation with increasing scan time. A possible explanation for this could be that respiration was faster in the beginning of the scan, and as the subject became relaxed, the respiratory frequency might have decreased. Specifically, in a situation where the respiratory frequency decreases over time but the amplitude stays stable, the intra-thoracic pressure during inspiration and expiration reaches lower extremes, i.e. the upslope and downslope on the respiratory volume curve becomes less steep. This results in a smaller respiratory-induced variation in right ventricular EDV and, thereby, decreased respiratory-induced variation in LVEDV.

However, to verify if this is cause of the decreasing variation in LVEDV with increasing scan time, an investigation of the respiratory pattern during acquisition is necessary. Another explanation for the tendency of variation in LVEDV to decrease could be found in the image quality. A downside to the 4.5-minute acquisition compared to 25 minutes was a subjective decrease in image quality that might have affected the accuracy of the segmentation of the endocardial border. There was an opposite non-significant trend that the LVEDV slightly increased with increased scan time, and that could have been a result of lower image quality for shorter scan time. If the absolute difference between the LVEDV in mid inspiration and mid expiration was equally large, the percentage difference could have been higher with shorter scan time.

Measuring the respiratory variation in LV area or diameter can be done with a 2D imaging technique that requires much shorter acquisition time than 3D whole-heart acquisition. Additionally, initial experience with 2D and 3D golden-angle radial acquisition showed that the image quality was better with 2D imaging. So why should we use the LVEDV, obtained from a time consuming 3D acquisition, as a measure of respiratory variation in cardiac dimensions? It is speculated that LVEDV is more reproducible and robust than measurements of LV area or diameter. Any 2D CMR imaging technique requires planning of the slice position and image plane angulation. If the SA slice is not perpendicular to the myocardium this leads to errors in measurement of the ventricular area or diameter and thereby variability in measurements of the respiratory variation. There might also be position-dependent variation in movement along the septum during respiration, and a slice position further towards the base might measure a different respiratory variation than a slice position further towards the apex. Additionally, the position of the heart inside the thoracic cavity might vary between mid inspiration and mid expiration. A study has shown that respiratory navigators measure a hysteretic effect in diaphragm position between inspiration and expiration (70). Since the heart rests on the diaphragm, the through-plane motion in the 2D slice could lead to measurements of area or diameter in different parts of the heart between mid inspiration and mid expiration. LVEDV measured from free breathing whole-heart imaging eliminates all these potential 2D issues, because the entire LV endocardial border is contributing to the measure.

LV volumes are a central part of the report from a CMR exam, and therefore it was an obvious choice to measure the respiratory change in LVEDV in this work. However, the variation in LVEDV is only indirectly caused by respiration via the interventricular coupling and direct respiratory variation in the right ventricular diastolic filling. If the respiratory-induced variation in cardiac dimensions would be the central question of a CMR exam, would measuring the right ventricular EDV provide the same respiratory variation as in the LVEDV, or would it be higher? In addition, if respiratory-induced variation in LVEDV were higher, would it thereby be easier to distinguish healthy from

disease? This remains an unanswered question that would be interesting to investigate in the future.

Measurement of the respiratory variation in LVEDV with free breathing whole-heart CMR has some potentially significant applications. First, it allows for visualization of the rather unique cardio-respiratory coupling and could be used for getting a better understanding of the normal cardio-respiratory physiology. Second, it can be used for distinguishing different types of diseases affecting the cardio-respiratory coupling, such as constrictive pericarditis and restrictive cardiomyopathy. Finally, it clearly emphasizes the importance of treating the inspiratory and expiratory phases differently. The heart might be at the same level in mid inspiration and mid expiration, but the internal cardiac dimensions are not. It is common in respiratory gated free breathing cardiac imaging to only consider diaphragm position in order to increase the data amounts in each bin. But mixing the inspiration and expiration can lead to motion blurring, especially around the septum. The first and second potential applications, however, require much more testing and potentially a gold standard and/or extensive normal material for reliable measures.

5.2 From volunteers to patients

For CMR, as well as other methodological developments, taking the step from imaging healthy volunteers to use in a clinical environment is a sizeable challenge. Patients can be less cooperative or have difficulties following instructions. Furthermore, and understandably, they might be worried, not feeling well, or simply experiencing hearing difficulties. Moreover, patients can have larger variations in heart rate and respiration. Another aspect of the step from volunteers to patients is the controlled manner in which data is acquired. Acquisition in healthy volunteers is often done by the researcher in a relaxed setting with plenty of time and only one goal. During clinical routine, the CMR technologists are often pressed for time and have many other acquisitions they need to do well, and the precision the researcher might display can often be unfeasible to achieve, regardless of the skill of the technologists.

Initial evaluations of CMR developments are typically undertaken in healthy volunteers, recruited within the researchers own network and are therefore likely to be young and well educated. As a group, healthy volunteers are therefore not necessarily representative of CMR patients. Thus, the method may require substantial adjustments to transition from volunteers to patients in a clinical environment.

In this work, measurements of respiratory variation in LVEDV proved to be challenging in patients since the original *k*-space based respiratory self-gating completely failed in distinguishing the respiratory cycles. The reason for that was likely that the band-pass filter was not able to capture the large frequency variations seen in many of the patients.

Another interesting outcome between Studies II and IV is the slight difference in respiratory-induced variation in LVEDV between volunteers and patients. Specifically, the variation in LVEDV was 8 % in patients compared to 6 % in healthy volunteers. Whether this difference has a physiological explanation, is due to the change in respiratory self-gating approach, or even if it is statistically different is not clear and requires further study. One argument for a physiological difference is that patients might have had faster breathing and, thereby, produced larger intra-thoracic pressure differences than healthy volunteers; this may be a reflection of whether they were worried or maybe experienced pain or discomfort. An argument for the change in self-gating technique would be that the projection based self-gating might be better at precisely distinguishing mid inspiration and mid expiration because it uses both phase and amplitude information.

Presently, it is not possible to make any conclusions about whether the respiratory-induced variation in LVEDV is higher in patients than healthy volunteers. More testing of the respiratory self-gating approach, and possibly in larger groups, is necessary. Additionally, it is crucial to test whether whole-heart free breathing 3D imaging is in fact capable of distinguishing between health and disease, and whether the technique is capable of differentiating between different types of diseases which affect the respiratory-induced variation in LVEDV.

5.3 Study limitations

At this point a potential new CMR imaging method has been developed for measuring the respiratory-induced variation in LVEDV, but the question of clinical value is still unanswered and much validation of the technique itself is still needed.

5.3.1 Gold standard

No gold standard exists for measuring the respiratory variation in cardiac dimensions. So how do we actually know that the measurements of respiratory variation are correct? Many studies report that they have found respiratory variation in LV dimensions and compare those to what others previously have published. Similarly, such an approach was used to interpret the results of Studies II and IV. Two of the major limitations to this way of evaluating the findings are the typically small study populations and that the methods used for measuring the variation differ from study to study. A gold standard might be created by measuring the respiratory variation with a number of different methods within a large group of healthy individuals. One possible approach could be to measure the respiratory pressure at the same time as measuring respiratory variation in cardiac dimensions. Indeed, the various methods for measuring the respiratory variation in cardiac dimensions also need to be compared and validated against each other. Some CMR methods for quantitative measurements are validated against a known quantity, e.g. flow measurements can be validated with a flow phantom. The cardio-respiratory

physiology is so complex, though, that a phantom imitating the flow/volume variations in response to pressure changes likely would not be able to account for all variables. But would it be necessary to measure the variation precisely? It might be enough to have a normal material as reference standard for a specific method as long as it can distinguish healthy from disease and in a reproducible manner.

5.3.2 Reproducibility and missing evaluations

Reproducibility of measuring left ventricular EDV and ESV with free breathing double golden-angle acquisition was done in Study I, but only for the cardiac variation and only in healthy volunteers. No reproducibility measurements were done for measuring respiratory variation in LVEDV. Therefore, conclusions about the robustness of the method cannot be drawn. Similarly, LVEDV measurements with free breathing CMR imaging were not evaluated in patients, which could be compared to gold standard 2D breath held cine. LV volumes in patients vary much more than in healthy volunteers and such evaluation might have uncovered some limitations in the method.

Taking the step from volunteers to patients in this work was done with the tiny double golden-angle radial trajectory instead of the original used in volunteers. The tiny trajectory was only tested in one volunteer in Study III before being applied in patients. The respiratory variation in LVEDV appeared to be slightly higher in patients than in healthy volunteers and there is no way of knowing if that was due to the change in trajectory, new projection-based respiratory self-gating strategy, or a physiological difference between the two groups.

To separate these three questions, the original and new trajectory could have been tested in healthy volunteers with the same respiratory self-gating. An attempt to eliminate the bias of changing the respiratory self-gating was made by evaluating the respiratory variation in LVEDV in patients with both self-gating methods. However, because the *k*-space based self-gating failed it was difficult to compare the results to healthy volunteers.

Clarification on the physiological differences between the healthy volunteer and patient groups might have been revealed with deeper investigation into the respiratory patterns. Inter-thoracic pressure is indirectly represented by the upslope and downslope of respiratory amplitude from bellows or projection-based self-gating signals. A steeper slope means higher intra-thoracic pressure (or lower in inspiration) and, theoretically, larger respiratory variation in LVEDV. Indication of respiratory pressure from upslope and downslope would only be comparable between Studies II and IV using the bellows signals, but could be correlated to the magnitude of LVEDV variation, and possibly provide some insight into the physiological traits of the two groups.

LVEDV measurements were done from manual segmentation of the endocardial border. Usually, experienced clinicians do this with help from programs with

semiautomatic segmentation tools. However, in this work manual segmentation was done by a relatively inexperienced engineer. The segmentations were corrected and approved by an experienced clinician, but it still raises some questions about bias. First, the segmentations were not blinded, but done in consecutive order. Second, there was a clear hypothesis that both the clinician and researcher were familiar with. The main worry was whether the results could have been exaggerated by confirmation bias. To eliminate potential bias, it would have been preferable to have the segmentations done by a blinded clinician. The in-house evaluations of initial CMR development is, however, common practice in many research groups, and, for proof-of-concept studies, might be good enough, as long as there is awareness of the potential bias.

5.3.3 Study populations

No more than 10 individuals were used in any of the studies. The focus has been on developing the free breathing 3D CMR method and the papers were intended as a proof-of-concept. This is a major step in every new development, but it is also a very early step and the small population sizes for both volunteers and patients provide no information about the robustness of the method. Much more research and extensive investigation is necessary for that.

Some limitations to both the healthy volunteer and patient groups are also worth mentioning. The healthy volunteers were recruited from the author's own network, and most were 25-35 years old and well educated. As mentioned, this might have made them better at following instructions than the general population. Furthermore, many of them were in excellent shape and, in combination with being young, might therefore have had more stable respiration and heart rhythm than the general healthy population. And finally, several of the volunteers were recruited within medical and biological research making them used to being in a hospital environment. All these combined may have led to overestimation of the performance of the CMR technique. This can be reflected in superb operator-volunteer cooperation, little variation within the group, and reduced variation within the respiration and heart rate during scan time. Overestimation may be attributed to the homogenous volunteer group, which might have concealed some of the critical limitations this method might have.

Patients in Study IV were recruited directly from the clinic, but all of them were outpatients. They were therefore not sick or weak enough to require hospitalization. As with the healthy volunteers, this could have led to a situation where the method was not evaluated in the full range of conditions that could be encountered in the clinical setting. Furthermore, it is not clear if there might have been a specific patient group or pathology where the imaging method would work sub-optimally.

5.4 What does the future for cardiac 5D cine imaging look like?

In this work free breathing whole-heart cardio-respiratory resolved cine imaging has been developed and evaluated in five dimensions, which consist of three image dimensions as well as the cardiac and respiratory cycles.

With this 5D whole-heart cine imaging, LV volumes were measured in different cardio-respiratory phase combinations. LV volumes during the cardiac cycle showed similar values and reproducibility as LV volumes measures with gold standard breath held 2D cine imaging. Respiratory-induced variation of 5-10 % was demonstrated in healthy volunteers for left ventricular EDV, diameter and area as well as in patients for LVEDV.

5D whole-heart cine imaging during free breathing with tiny double golden-angle radial acquisition shows potential, but is still in the proof-of-concept phase and there is a long way to go before it is ready for clinical use.

Are we actually ready for clinical 5D cardiac cine imaging or even 3D cardiac imaging in general? Image quality, image reconstruction time and partly acquisition time is still inferior to 2D breath held imaging. These factors need to be greatly improved before 3D cine imaging has a place in clinical CMR exams.

Acquisition time of 4.5 minutes has been demonstrated in this work for respiratory resolved cardiac cine imaging to measure LVEDV, but the image quality, though sufficient for segmentation, was rather poor. Some CMR techniques, like the XD-GRASP in combination with the spiral phyllotaxis trajectory, are showing promising results in image quality and acquisition times by combining parallel imaging with compressed sensing during image reconstruction to allowing for extensive undersampling. The major drawback on these image reconstruction techniques is the vast amount of data to be processed in an iterative manner, which places high requirements on the computational systems.

Better infrastructures for data handling as well as more powerful computers are needed to sustain free breathing 5D imaging with retrospective gating and cardio-respiratory binning, which requires acquisition and processing of data for many 3D image volumes. Graphical processing units and cloud based computing are features that may enable processing and image reconstruction of such data amounts, but the development is still in its initial phase. Additionally, sending the data to be processed externally in the “cloud” requires other considerations such as ensuring protection of privacy for the patients. However, eventually cloud based image reconstruction could become a part of the standard CMR exam. The necessary computational power increases rapidly, and it would likely be impractical for each hospital to have and maintain such a computational infrastructure. Collaborative research on image reconstruction techniques is made

difficult by the protected software of different vendors. It is likely that open-source reconstruction software and infrastructure that can be incorporated into online reconstruction in the clinic, such as the Gadgetron (71), will speed up the development by allowing for more collaboration among research groups.

Methods for respiratory self-gating are also fiercely being researched and will likely improve and allow for more precisely defining respiratory phase in the future. There seem to be less interest in cardiac self-gating because the ECG does a decent job. Cardiac self-gating might eventually be a part of the clinical routine, but probably further into the future than respiratory self-gating. In this work it was found that image quality varied among volunteers as well as patients. It was noted that part of it had to do with insufficient respiratory self-gating, and improvements in respiratory self-gating could potentially also improve image quality in 3D cardiac imaging.

Another improvement that might increase image quality would be to shorten the acquisition time. Longer acquisitions provide a greater risk that the patient moves which would cause blurring or artifacts in the images. A shorter acquisition time could also ensure a smaller variation in respiratory and cardiac frequencies, which would make it easier for self-gating techniques to extract the correct information.

There is also much development remaining regarding trajectory corrections. The MRI system is far from perfect, and eddy currents and gradient delays poses an obstacle for good image quality. Eddy currents were reduced with the trajectory proposed in Study III, but more evaluation of the tiny double golden-angle radial trajectory in comparison to existing trajectories remains. Gradient delays cause *k*-space lines to be positioned slightly wrong and result in image artifacts. Initial testing of simple gradient delay correction in this work showed that gradient delays had little or no visual impact on *in vivo* images, but it is likely that it still provides some streaking in radial imaging. In the future, many of these system imperfections might collectively be corrected for by emerging techniques using a gradient-impulse response function (GIRF) measured once per few months for individual scanners (72). Such a correction could have a potential impact on non-Cartesian trajectories, as they are more sensitive to system imperfections. It is possible that GIRF or other methods may pave the way toward the future for such systems.

In general, free breathing 3D cardiac cine imaging resolved over the cardiac cycle likely has a potential future in CMR. There is a clinical need for replacing the 2D breath held standard and to simplify the acquisition as well as making the post-processing more flexible. Combined with good multi-planar reformatting software, 3D cardiac cine imaging has the potential to be a tool for the clinician to gain a deeper understanding of each individual patient's heart. No two hearts are the same and they should not be treated as such. Especially patients with congenital heart disease could potentially benefit from free breathing 3D cardiac cine and possibly also patients under general anesthesia.

However, free breathing cardiac cine imaging will likely not replace the breath held 2D variants until some of the essential issues with infrastructure, image quality, and respiratory self-gating are solved. A free breathing 3D cardiac cine imaging comprising 3D acquisition retrospectively resolved over the cardiac phase dimension has a clear place in the standard clinical imaging package as it would potentially benefit all cardiac patients. Cardiac resolved 3D imaging could even be done with prospective respiratory gating to decrease the data amount and possibly image reconstruction times.

The 5D cardio-respiratory resolved cine imaging during free breathing might be a little further down the road than the cardiac resolved only 3D imaging, and it will likely not be a part of the standard imaging package, but a special feature applied in specific patients like those with pericardial disease.

The concept of 5D cardio-respiratory resolved cine imaging during free breathing has been shown to work well in both healthy volunteers and patients. It has potential diagnostic value, and the future challenges are possible to overcome. It is not unreasonable to envision a future where such technique will have an impact on diagnostic cardiovascular magnetic resonance imaging.

Chapter 6
Conclusions

The results from this work show that it is possible to image the heart in five dimensions with a novel CMR imaging technique combining whole-heart free-running acquisition with retrospective binning of cardiac and respiratory phases. It was possible to measure both cardiac and respiratory motion-induced variations in LVEDV, and study the two dimensions separately.

This work illustrates the importance of treating the mid inspiration and mid expiration phases separately for data binning because the left-ventricular chamber varies in size and shape between these two phases.

Specific conclusions for Studies I-IV were:

I. Measurements of left ventricular volumes in end diastole and end systole with free breathing 3D radial acquisition and retrospective respiratory self-gating in healthy volunteers showed no difference in absolute values as well as test-retest variation compared to standard 2D breath held cine imaging.

II. Respiratory-induced variation in LVEDV was 5-6 % compared to maximum LVEDV in mid expiration. 4.5-, 9-, and 25-minute acquisition durations were tested, and there were no differences in respiratory-induced variation in LVEDV between different durations of acquisition.

III. Eddy current-related artifacts were reduced by modifying and generalizing the double golden-angle radial trajectory to produce tiny angle increments between consecutive spokes. Image uniformity in phantoms and a healthy volunteer was improved.

IV. Respiratory-induced variation in LVEDV was demonstrated in patients with a projection-based respiratory self-gating and 10 minutes acquisition, whereas the *k*-space based respiratory self-gating, used in volunteers, failed to measure the variation. Respiratory-induced variation in LVEDV in patients was 8 %.

Acknowledgements

It takes a village… Which is also true for getting through 4 years of PhD studies!

I have been privileged with tremendous support from colleagues, friends and family, without whom, this thesis would not have been possible.

I would like to thank my main supervisor, Andreas Sigfridsson, for guidance and support. Andreas, your support, open door, discussions and numerous explanations of MR physics (occasionally more than once!) have provided a secure place for my professional and personal development into an independent researcher and stronger person. Thank you.

Thanks to my co-supervisors Martin Ugander and Kenneth Caidahl. Martin, thank you for tremendous academic discussions and patience, especially in situations where we did not see eye-to-eye. Kenneth, thank you for always finding time in your busy schedule for mentoring and guidance in difficult situations.

Thanks to my awesome colleagues in the Karolinska CMR group for creating a warm and fun workplace. Thanks to technologists Jenny Rasck and Sofie Olsson, for your help and always-positive attitudes, even during scanner battles for the greater good of research.

Especially, I would like to thank to my fellow PhD students, Alexander Fyrdahl and Jannike Nickander. You two have been the golden angels (as I have mistakenly written several times!) keeping me sane, especially in the final phases of experiments, manuscript preparations and thesis writing. Alex, thank you for emotional support and practical help in basically all aspects of the work behind this thesis! I appreciate our deep conversations about everything from MR physics to how the best steak is cooked. Jannike, thank you for supporting me through ups and downs, for challenging my ways of thinking and celebrations of our success points.

Thanks to Adrienne Campbell-Washburn and Michael Hansen for inviting me into their research group at the NIH and expanding my scientific horizon. Thank you both for personal support and insightful discussions.

To Juan Acosta, my wonderful partner. You have been my greatest supporter in the final sprint of this race and endured all the mood swings and anxieties, and I thank you for an endless amount of patience and home cooked meals.

To all my amazing friends in Stockholm: Tiago, Ariel, Greta, Theresa, Magali and Elira, in Copenhagen: Louise and Nives, in Washington: Amy and Eleni, and in Toronto: Hanif. Thank you all for the loving ears and support! I have needed every one of you to keep me connected to the real world, for laughing with me, late night salsa dancing, hiking, traveling, dinners and much more. Thank you.

Thanks to my mother, Marie and brother, Jesper. Mor, thank you for preparing me for this difficult and exciting journey and always being available when I need a fresh perspective or a pair of ears. Jesper, thanks for always challenging me and having my back when needed. I love you both.

Finally, to my father, Steffen, and to whom this thesis has been dedicated. Far, you have from since I can remember put me on the path of science by stimulating my curiosity. Our many hikes discovering plants, insects and birds, late nights looking at stars through your telescope, evenings watching documentaries and discussing society issues have all provoked my interest in science and led to a desire of deeper understanding. I love you and I will support you through anything the future holds.

References

1. Harvey W, Leake CD. Exercitatio anatomica de motu cordis et sanguinis in animalibus. 1st ed. Springfield, IL: Thomas; 1928.

2. Burton-Opitz R. The flow of blood in the external jugular vein. Am J Physiol 1902;7:435–459.

3. Harrison DC, Goldblatt A, Braunwald E, Glick G, Mason DT. Studies on cardiac dimensions in intact, unanesthetized man. Circ Res 1963;13:448–467.

4. Schünke M, Schulte E, Schumacher U, Ross L, Lamperti E. Thieme Atlas of anatomy. Stuttgard: Thieme; 2006.

5. Farah CS, Reinach FC. The troponin complex and regulation of muscle contraction. Faseb J 1995;9:755–767.

6. Persson PB. Modulation of cardiovascular control mechanisms and their interaction. Physiol Rev 1996;76:193–244.

7. Wiggers C. Studies on the consecutive phases of the cardiac cycle. Am J Physiol 1921;56:415–438.

8. Einthoven W. Physiology or Medicine 1922-1941. Amsterdam: Elsevier publishing company; 1965.

9. Wiggers C, Katz L. The contour of the ventricular volume curves under different conditions. Am J Physiol 1922;58:439–475.

10. Boron WF, Boulpaep EL. Medical physiology: a cellular and molecular approach. Philadelphia, PA: Saunders/Elsevier; 2009.

11. Patterson SW, Starling EH. On the mechanical factors which determine the output of the ventricles. J Physiol 1914;48:357–379.

12. Andresen MC, Kunze DL. Nucleus tractus solitarius – Gateway to neural circulatory control. Annu Rev Physiol 1994;56:93–116.

13. Coleridge HM, Coleridge JCG. Pulmonary reflexes: neural mechanisms of pulmonary defense. Annu Rev Physiol 1994;56:69–91.

14. Mills JN. Variability of the vital capacity of the normal human subject. J Physiol 1949;110:76–82.

15. Fowler WS. Lung function studies; the respiratory dead space. Am J Physiol 1948;154:405–416.

16. Weber KT, Janicki JS, Shroff S, Fishman AP. Contractile mechanics and interaction of the right and left ventricles. Am J Cardiol 1981;47:686–695.

17. Francone M, Dymarkowski S, Kalantzi M, Rademakers FE, Bogaert J. Assessment of ventricular coupling with real-time cine MRI and its value to differentiate constrictive pericarditis from restrictive cardiomyopathy. Eur Radiol 2006;16:944–951.

18. Garcia MJ. Constrictive pericarditis versus restrictive cardiomyopathy? J Am Coll Cardiol 2016;67:2061–2076.

19. Janicki JS, Weber KT. The pericardium and ventricular interaction, distensibility, and function. Am J Physiol 1980;238:494-503.

20. Kusunose K, Dahiya A, Popović ZB, Motoki H, Alraies MC, Zurick AO, Bolen MA, Kwon DH, Flamm SD, Klein AL. Biventricular mechanics in constrictive pericarditis comparison with restrictive cardiomyopathy and impact of pericardiectomy. Circ Cardiovasc Imaging 2013;6:399–406.

21. Myers RBH, Spodick DH. Constrictive pericarditis: Clinical and pathophysiologic characteristics. Am Heart J 1999;138:219–232.

22. Yusuf SW, Hassan SA, Mouhayar E, Negi SI, Banchs J, O 'gara PT. Pericardial disease: A clinical review. Expert Rev Cardiovasc Ther 2016;144:525–539.

23. Adler Y, Charron P, Imazio M, et al. 2015 ESC Guidelines for the diagnosis and management of pericardial diseases: The Task Force for the Diagnosis and Management of Pericardial Diseases of the European Society of Cardiology (ESC). Eur Heart J 2015;36:2921–2964.

24. Giorgi B, Mollet NRA, Dymarkowski S, Rademakers FE, Bogaert J. Clinically suspected constrictive pericarditis: MR imaging assessment of ventricular septal motion and configuration in patients and healthy subjects. Radiology 2003;228:417–424.

25. Cummings KW, Green D, Johnson WR, Javidan-Nejad C, Bhalla S. Imaging of pericardial diseases. Semin Ultrasound, CT MRI 2016;37:238–254.

26. Rabi II, Zacharias JR, Millman S, Kusch P. A new method of measuring nuclear magnetic moment. Phys Rev 1938;53:318.

27. Levitt MH. Spin dynamics: Basics of nuclear magnetic resonance. 2nd ed. New York, NY: Wiley; 2008.

28. Bloch F. Nuclear induction. Phys Rev 1946;70:460.

29. Hahn EL. An accurate nuclear magnetic resonance method for measuring spin-lattice relaxation times. Phys Rev 1949;76:145–146.

30. Lauterbur PC. Magnetic resonance zeugmatography. Pure Appl Chem 1974;40:149.

31. Kumar A, Welti D, Ernst RR. NMR Fourier zeugmatography. J Magn Reson 1975;18:69–83.

32. Moran PR. A flow velocity zeugmatographic interlace for NMR imaging in humans. Magn Reson Imaging 1982;1:197–203.

33. Messroghli DR, Niendorf T, Schulz-Menger J, Dietz R, Friedrich MG. T1 mapping in patients with acute myocardial infarction. J Cardiovasc Magn Reson 2003;5:353–359.

34. Giri S, Chung Y-C, Merchant A, Mihai G, Rajagopalan S, Raman S V, Simonetti OP. T2 quantification for improved detection of myocardial edema. J Cardiovasc Magn Reson 2009;11:56.

35. Edelman RR, Manning WJ, Burstein D, Paulin S. Coronary arteries: breath-hold MR angiography. Radiology 1991;181:641–643.

36. Sechtem U, Pflugfelder PW, White RD, Gould RG, Holt W, Lipton MJ, Higgins CB. Cine MR imaging: Potential for the evaluation of cardiovascular function. Am J Roentgenol 1987;148:239–246.

37. Goldman MR, Brady TJ, Pykett IL, Burt CT, Buonanno FS, Kistler JP, Newhouse JH, Hinshaw WS, Pohost GM. Quantification of experimental myocardial infarction using nuclear magnetic resonance imaging and paramagnetic ion contrast enhancement in excised canine hearts. Circulation 1982;66:1012–1016.

38. Pohost GM, Ratner A V. Nuclear magnetic resonance: Potential applications in clinical cardiology. JAMA 1984;251:1304–1309.

39. Utz J, Herfkens R, Heinsimer J, Bashore T, Califf R, Glover G, Pelc N, Shimakawa A. Cine MR determination of left ventricular ejection fraction. Am J Roentgenol 1987;148:839–843.

40. Sechtem U, Pflugfelder PW, Gould RG, Cassidy MM, Higgins CB. Measurement of right and left ventricular volumes in healthy individuals with cine MR imaging. Radiology 1987;163:697–702.

41. Glover GH, Pelc NJ. A rapid gated cine MRI technique. In: Kressel HY, editor. Magnetic Resonance Annual. New York, NY: Raven Press; 1988. pp. 299–333.

42. Wang Y, Riederer SJ, Ehman RL. Respiratory motion of the heart: Kinematics and the implications for the spatial resolution in coronary imaging. Magn Reson Med 1995;33:713–719.

43. McConnell M V, Kahsgiwala VC, Savord BJ, Chen MH, Chuang ML, Edelman RR, Manning WJ. Comparison of respiratory suppression methods and navigator locations for MR coronary angiography. Am J Roentgenol 1997;168:1369–1375.

44. Block KT, Chandarana H, Milla S, et al. Towards routine clinical use of radial stack-of-stars 3D gradient-echo sequences for reducing motion sensitivity. J Korean Soc Magn Reson Med 2014;18:87–106.

45. Ferreira PF, Gatehouse PD, Mohiaddin RH, Firmin DN. Cardiovascular magnetic resonance artefacts. J Cardiovasc Magn Reson 2013;15:41.

46. Wang Y, Christy PS, Korosec FR, Alley MT, Grist TM, Polzin JA, Mistretta CA. Coronary MRI with a respiratory feedback monitor: The 2D imaging case. Magn Reson Med 1995;33:116–121.

47. Kilner PJ, Geva T, Kaemmerer H, Trindade PT, Schwitter J, Webb GD. Recommendations for cardiovascular magnetic resonance in adults with congenital heart disease from the respective working groups of the European Society of Cardiology. Eur Heart J 2010;31:794–805.

48. Chan RW, Ramsay EA, Cunningham CH, Plewes DB. Temporal stability of adaptive 3D radial MRI using multidimensional golden means. Magn Reson Med 2009;61:354–363.

49. Hansen MS, Sørensen TS, Arai AE, Kellman P. Retrospective reconstruction of high temporal resolution cine images from real-time MRI using iterative motion correction. Magn Reson Med 2012;68:741–750.

50. Winkelmann S, Schaeffter T, Koehler T, Eggers H, Doessel O. An optimal radial profile order based on the golden ratio for time-resolved MRI. IEEE Trans Med Imaging 2007;26:68–76.

51. Piccini D, Littmann A, Nielles-Vallespin S, Zenge MO. Spiral phyllotaxis: the natural way to construct a 3D radial trajectory in MRI. Magn Reson Med 2011;66:1049–1056.

52. Bieri O, Markl M, Scheffler K. Analysis and compensation of eddy currents in balanced SSFP. Magn Reson Med 2005;54:129–137.

53. Markl M, Leupold J, Bieri O, Scheffler K, Hennig J. Double average parallel steady-state free precession imaging: Optimized eddy current and transient oscillation compensation. Magn Reson Med 2005;54:965–974.

54. Peters DC, Korosec FR, Grist TM, Block WF, Holden JE, Vigen KK, Mistretta CA. Undersampled projection reconstruction applied to MR angiography. Magn Reson Med 2000;43:91–101.

55. Feinberg DA, Hale JD, Watts JC, Kaufman L, Mark A. Halving MR imaging time by conjugation: Demonstration at 3.5 kG. Radiology 1986;161:527–531.

56. O'Sullivan JD. A fast sinc function gridding algorithm for fourier inversion in computer tomography. IEEE Trans Med Imaging 1985;4:200–207.

57. Dutt A, Rokhlin V. Fast Fourier transforms for nonequispaced data. SIAM J Sci Comput 1993;14:1368–1393.

58. Fessler JA, Sutton BP. Nonuniform fast Fourier transforms using min-max interpolation. IEEE Trans Signal Process 2003;51:560–574.

59. Pruessmann KP, Weiger M, Börnert P, Boesiger P. Advances in sensitivity encoding with arbitrary k-space trajectories. Magn Reson Med 2001;46:638–651.

60. Ehman R, McNamara M, Pallack M, Hricak H, Higgins C. Magnetic resonance imaging with respiratory gating: techniques and advantages. Am J Roentgenol 1984;143:1175–1182.

61. Santelli C, Nezafat R, Goddu B, Manning WJ, Smink J, Kozerke S, Peters DC. Respiratory bellows revisited for motion compensation: Preliminary experience for cardiovascular MR. Magn Reson Med 2011;65:1097–1102.

62. McConnell MV, Khasgiwala VC, Savord BJ, Ming Hui Chen, Chuang ML, Edelman RR, Manning WJ. Comparison of respiratory suppression methods and navigator locations for MR coronary angiography. Am J Roentgenol 1997;168:1369–1375.

63. Ehman RL, Felmlee JP. Adaptive technique for high-definition MR imaging of moving structures. Radiology 1989;173:255–263.

64. McConnell MV., Khasgiwala VC, Savord BJ, Chen MH, Chuang ML, Manning WJ, Edelman RR. Prospective adaptive navigator correction for breath-hold MR coronary angiography. Magn Reson Med 1997;37:148–152.

65. Feng L, Axel L, Chandarana H, Block KT, Sodickson DK, Otazo R. XD-GRASP: Golden-angle radial MRI with reconstruction of extra motion-state dimensions using compressed sensing. Magn Reson Med 2015;75:775–788.

66. Sigfridsson A, Kvitting JPE, Knutsson H, Wigström L. Five-dimensional MRI incorporating simultaneous resolution of cardiac and respiratory phases for volumetric imaging. J Magn Reson Imaging 2007;25:113–121.

67. Fredrickson JO, Wegmüller H, Herfkens RJ, Pelc NJ. Simultaneous temporal resolution of cardiac and respiratory motion in MR imaging. Radiology 1995;195:169–175.

68. Thompson RB, McVeigh ER. Cardiorespiratory-resolved magnetic resonance imaging: Measuring respiratory modulation of cardiac function. Magn Reson Med 2006;56:1301–1310.

69. Wu Y, Wan Q, Zhao J, Liu X, Zheng H, Chung Y-C, Chen Y. Improved workflow for quantifying left ventricular function via cardiorespiratory-resolved analysis of free-breathing MR real-time cines. J Magn Reson Imaging 2017;46:905–914.

70. Nehrke K, Börnert P, Manke D, Böck JC. Free-breathing cardiac MR imaging: Study of implications of respiratory motion - initial results. Radiology 2001;220:810–815.

71. Hansen MS, Sørensen TS. Gadgetron: an open source framework for medical image reconstruction. Magn Reson Med 2013;69:1768–1776.

72. Campbell-Washburn AE, Xue H, Lederman RJ, Faranesh AZ, Hansen MS. Real-time distortion correction of spiral and echo planar images using the gradient system impulse response function. Magn Reson Med 2016;75:2278–2285.